Journal Pre-proof

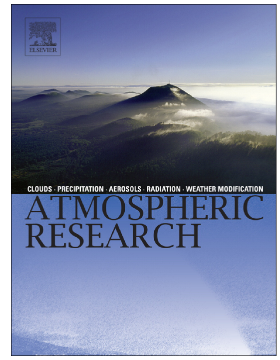

Lightning activity and its associations with cloud structures in a rainstorm dominated by warm precipitation

Ze Liu, Dong Zheng, Fengxia Guo, Yang Zhang, Yijun Zhang, Chong Wu, Haonan Chen, Songyu Han

PII: S0169-8095(19)31226-8

DOI: https://doi.org/10.1016/j.atmosres.2020.105120

Reference: ATMOS 105120

To appear in: *Atmospheric Research*

Received date: 17 September 2019

Revised date: 20 June 2020

Accepted date: 27 June 2020

Please cite this article as: Z. Liu, D. Zheng, F. Guo, et al., Lightning activity and its associations with cloud structures in a rainstorm dominated by warm precipitation, *Atmospheric Research* (2019), https://doi.org/10.1016/j.atmosres.2020.105120

Lightning activity and its associations with cloud structures in a rainstorm dominated by warm precipitation

Ze Liu[a,b,1], Dong Zheng[a,*,1], Fengxia Guo[b,*], Yang Zhang[a], Yijun Zhang[c], Chong Wu[a], Haonan Chen[d,e], Songyu Han[f]

a. State Key Laboratory of Severe Weather/Laboratory of Lightning Physics and Protection Engineering, Chinese Academy of Meteorological Sciences, Beijing, China

b. Key Laboratory of Meteorological Disaster, Ministry of Education (KLME)/ Joint International Research Laboratory of Climate and Environment Change (ILCEC)/Collaborative Innovation Center on Forecast and Evaluation of Meteorological Disasters (CIC-FEMD)/ Key Laboratory for Aerosol-Cloud-Precipitation of China Meteorological Administration, Nanjing University of Information Science & Technology, Nanjing 210044, China

c. Institute of Atmospheric Sciences, Fudan University, Shanghai, China

d. NOAA/Earth System Research Laboratory, Boulder, CO 80305, USA

e. Cooperative Institute for Research in the Atmosphere, Fort Collins, CO 80523, USA

f. Zhejiang Meteorological Information Network Center，Hangzhou，China

[*] Corresponding author: zhengdong@cma.gov.cn (D. Zheng); guofx@nuist.edu.cn (F. Guo)

[1] These authors contributed equally to this work, they are the co-first authors.

Highlights:

- Investigating electrical characteristics in a rainstorm dominated by warm cloud precipitation is novel.

- In this rainstorm, lightning discharges predominately occurred in areas featuring dry snow and relatively weak precipitation.
- The lightning discharges spatially deviate from the origin area of charging; the cause of this is discussed.

Abstract: Lightning activity and its associations with cloud structures during a rainstorm dominated by warm cloud precipitation were studied in Guangdong, China on May 7, 2017, using three-dimensional lightning location and polarimetric radar data. The overall convection and lightning activities of the rainstorm were weak. The rainstorm generally showed a typical tripolar charge structure with the main negative charge core located between the −15 and −8 °C environmental isotherms in the first 4 h. The height of the charge regions clearly decreased after this period, with the main negative charge core being below the –8 °C isotherm. Lightning discharges were more concentrated in areas featuring relatively weak convection and relatively low precipitation intensity. Most of the locations with lightning discharges were dominated by dry aggregated snow and weak updrafts and downdrafts. This investigation demonstrated that the lightning discharges were spatially separated from the area of origin of charging in this rainstorm. It is proposed that, with weak convection in the rainstorm, the charging rate was lower than the speed of charge transfer from the area of origin, causing a relatively low charge density and a low frequency of lightning in the area of origin of charging. Meanwhile, the aggregation of small charged particles in regions away from the area of origin of charging might be conducive to the formation of a relatively high charge density and therefore relatively frequent lightning flashes. This situation is different from a typical

thunderstorm with strong convection.

Keywords: rainstorm, convection, precipitation, lightning activity, hydrometeors

1. Introduction

Different weather systems often display variations in their lightning activities. For example, in typical thunderstorms and climate statistics, positive cloud-to-ground (PCG) lightning usually accounts for ~10% of the total cloud-to-ground (CG) lightning (Liu et al., 2011; Rudlosky and Fuelberg, 2010; Zheng et al., 2010), but the ratio of PCG lightning in severe thunderstorms is relatively high, even greater than 50% (MacGorman et al., 1989; Soula et al., 2004; Zheng and MacGorman, 2016). Winter thunderstorms may also produce high-proportion and large-current PCG lightning (Suzuki, 1992; Takeuti et al., 1976; Zheng et al., 2019a). Typical thunderstorms usually have tripolar charge structures (Williams, 1989), while some severe thunderstorms may have inverted charge structures (Rust et al., 2005; Zheng and MacGorman, 2016; Zheng et al., 2009). In typical or severe thunderstorms, the most active lightning discharges are usually distributed in or around the regions characterized by the strong kinematics, because of the dependence of charging process on the rebounding collisions between ice-phase particles under the influence of airflow; while in the regions away from convection, the lightning flashes are usually less frequent and spatially dispersed (Bruning and MacGorman, 2013; Carey, et al., 2005; Feng et al., 2007; Liu et al., 2001; López et al., 1990; Ribaud et al., 2016; Zhang et al., 2017; Zheng and MacGorman, 2016; Zheng et al., 2010).

For storms yielding heavy rainfall (i.e., rainstorms), their precipitation characteristics and triggering and maintenance mechanisms are often the focus of research, but their electrical attributes and characteristics have received less attention.

In this study, we investigated lightning activity in an extraordinary rainstorm that occurred near the Pearl River Delta in Guangdong, China on May 7, 2017 (Beijing time, the same below). The rainstorm yielded extreme rainfall in the Pearl River Delta, with a maximum recorded precipitation of 446.6 mm, but a relatively low lightning flash rate, which prompted us to explore the relationship between its lightning activity and precipitation structure.

2. Data and methodology

2.1. Observations and data

In the analysis, 3-D lightning location data, CG flash observation data, and polarimetric radar observation data were mainly used. They are introduced as follows.

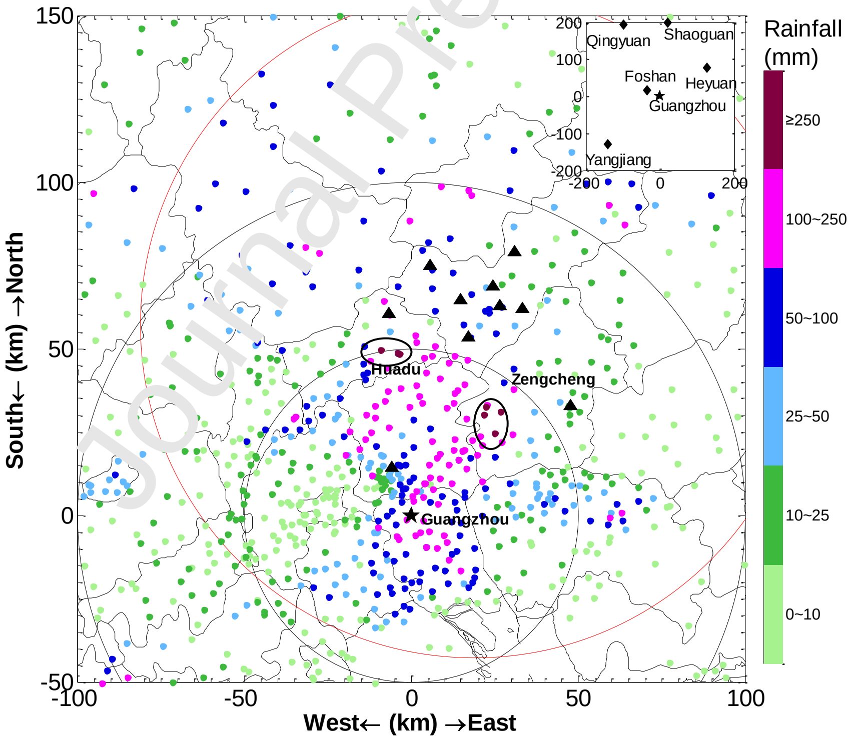

Fig. 1. Distribution of observing systems and cumulative precipitation from 20:00:00 on 6 May 2017 to 20:00:00 on May 7, 2017 (Beijing time, observed by ground-based automatic weather stations). The origin of the distance coordinate is located based on the position of the Guangzhou polarimetric radar (113.3553°E, 23.0039°N), which is

marked by the black star. The coordinates used in the following figures follow this definition. Solid dots show the positions of the automatic weather stations and their colors express the recorded cumulative precipitation, which is indicated by the color bar. Two black ellipses represent two precipitation centers with a cumulative precipitation greater than 250 mm; they are located in Huadu and Zengcheng, two districts in Guangzhou. The black triangles indicate the 10 substations in the Low-frequency E-field Detection Array (LFEDA). The red circle indicates the 100 km range of the LFEDA network center, and the two black concentric circles centered on the Guangzhou polarimetric radar indicate 50 and 100 km ranges from the radar center. The symbols in the following figures are the same. The small graph in the upper right corner shows the locations of the 6 radars that were used for the wind-field retrieval.

a. 3-D lightning location observation

The 3-D lightning location data were provided by the Low-Frequency E-field Detection Array (LFEDA), which consists of 10 stations (Fig. 1) and was developed by the Chinese Academy of Meteorological Sciences. The LFEDA detects the electric field change caused by lightning discharge in the 160–600 kHZ frequency band and locates the 3-D position and time of the discharge event associated with the electric field change pulse using the time of arrival method. Thus, we call the located source from the LFEDA the lightning pulse discharge events (LPDEs). More introduction on the LFEDA and its data application can be found in Chen et al. (2019), Fan et al. (2018), Shi et al. (2017), and Zheng et al. (2019b). In the estimation of the performance of the LFEDA based on artificially triggered lightning flashes (TLFs), the LFEDA detected 100% TLFs and 95% return strokes with the average location error of 102 m (Shi et al., 2017). For the detection of a lightning flash causing people's death, the LFEDA gave the 3-D spatial distribution of the lightning discharge process and located 7 return strokes with an average error of approximately 27 m (Fan et al., 2018).

The analysis referred to the LFEDA observation data between 00:00:00 and 12:00:00 on May 7, 2017. We chose the LPDEs whose located heights were less than 20 km and their chi-square goodness-of-fit values less than 10. The LPDEs were then grouped into flashes. A potential flash LPDE should occur within *t*1 s of the previous LPDE and within *t*2 s and *d* km of any other flash LPDE. The idea referred to the flash algorithm in the Lightning Mapping Array (MacGorman et al., 2008; Zheng and MacGorman, 2016; Zheng et al., 2019a), but the specific parameters were tested and adjusted for the LFEDA. For this analysis process, after comparing the flashes determined by this idea with multiple combinations of parameters and judged by humans, the parameters were determined as *t*1=0.4 s, *t*2=0.6 s, and *d*=4 km. The flashes to the analysis contained at least five LPDEs to exclude the effects of discrete points. The first LPDE in a lightning flash is roughly regarded as the initiation of flash (Zheng et al., 2019b).

LFEDA can locate the initial leader during the preliminary breakdown process of some lightning flashes. Zheng et al. (2019b) used LFEDA's locations to analyze the properties of negative initial leaders (NILs) during two thunderstorms in Guangdong and their associations with the initial positions. In their study, referring to the directions of the NILs and their initiation positions, they suggested the general charge structures of the thunderstorms. We will employ this method in this study. Lightning is typically initiated in a strong electric field, and two leaders with different polarities propagate towards the charge regions with opposite polarities to the leaders (Coleman et al., 2003; Shao and Krehbiel, 1996. Zhang et al., 2006a). The NIL is initiated near the edge of the negative charge region and develops towards the positive charge core, with relatively obvious vertical orientation. In some studies, the end of the NIL is determined to be the turning position where the leader's propagation direction changes to be predominantly horizontal (Bitzer et al., 2013; Shao and Krehbiel, 1996; Wu et al., 2015; Zheng et al., 2018, 2019b). Therefore, the initiation position of an NIL can be roughly regarded as the edge of the negative charge core. Fig. 2 shows the 3-D location of the NIL of a lightning flash. The NIL was initiated at approximately 6.6 km and developed to 7.9 km within approximately 3 ms, indicating it is an upward NIL (UNIL).

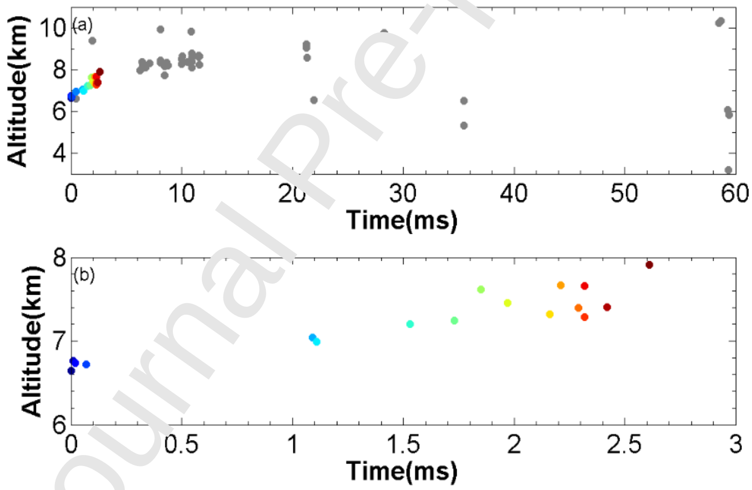

Fig. 2. A flash occurring at 04:12:08 on May 7, 2017 as an example to show the locations of the LPDEs associated with a negative initial leader (NIL). (a) LPDE height versus time; the colored dots indicate the NIL. (b) Enlarged display of the LPDEs associated with the NIL.

b. CG lightning data

The CG lightning data come from the Guangdong Lightning Location System (GDLLS), which was built and is operated by the State Grid Electric Power Research

Institute. Based on GDLLS's detection of artificially TLFs and natural lightning flashes striking tall structures in Guangzhou, Chen et al. (2012) evaluated the detection efficiency of the GDLLS for return stroke and CG lightning to be 60% and 94%, respectively. The return stroke records with peak current peak less than 10 kA were excluded to avoid the misinterpretation of cloud lightning, and then the return strokes were grouped into CG flashes using the criteria that adjacently located return strokes for one flash should occur within an interval of 0.5 s and at a distance of 10 km (Cummins et al., 1998; Zheng et al., 2016).

c. Radar data and processing

The S-band polarimetric radar in Guangzhou (Fig. 1) provided information on the precipitation structure of the rainstorm process. For the convenience of analysis, the original polar coordinate data from the radar was converted into rectangular coordinate data with a horizontal resolution of 0.25 km × 0.25 km and a vertical resolution of 0.5 km by interpolation. In addition to the traditional variable of reflectivity factor at horizontal polarization, the Guangzhou Radar provided additional variables such as the differential reflectivity, specific differential phase (computed from the differential phase shift) and copolar cross-correlation coefficient. The information on the classification of hydrometeors was obtained using software developed by the Chinese Academy of Meteorological Sciences (Wu et al., 2018), which referred to the hydrometeor classification algorithm developed by Park et al. (2009). Additionally, the observation of the polarimetric radar was used to obtain the surface precipitation using the retrieval algorithm introduced by Chen et al. (2017). Based on the dual-radar 3-D wind-field retrieval technique suggested by Luo et al. (2012), a total of six radars (Fig. 1), including the Guangzhou, Yangjiang (111.9792°E, 21.8450°N), Shaoguan (113.5655°E, 24.7906°N), Qingyuan (112.4003°E, 24.7325°N), Foshan (113.0103°E, 23.1444°N) and Heyuan (114.6069°E, 23.6903°N) radars, are used to get the wind field information in some areas of the rainstorm system.

d. Precipitation data from automatic weather stations

The cumulative precipitation data from 20:00:00 on 6 May 2017 to 20:00:00 on May 7, 2017 were provided by the automatic weather stations; their locations and recorded values are shown in Fig. 1.

2.2. Overview of the rainstorm process

The core area of precipitation during the rainstorm process is the Pearl River Delta in Guangdong Province and its surrounding areas. There were 142 automatic weather stations with a 24-hour cumulative rainfall of more than 50 mm; seven of them located in the east of Huadu district and west of Zengcheng district recorded cumulative precipitation exceeding 250 mm (see Fig. 1), with the documented maximum surface rainfall of 446.6 mm. By checking the radar data, this maximum rainfall came from approximately 10-h precipitation accumulation. Previous studies on this rainstorm showed that the atmospheric stratification prior to this storm featured weak convective inhibition, low lifting condensation levels, moderate convective available potential energy, deep warm layer and moist southerly flow, the height of strong radar reflectivity was relatively low, and the heavy precipitation dominantly consisted of high concentration of small raindrops, suggesting the rainstorm was dominated by warm cloud precipitation (Fu et al., 2018; Tian et al., 2018; Xu et al., 2018; Zeng et al., 2018; Zhang et al., 2018; Zhang et al., 2019).

Fig. 3 shows the composite reflectivity of the Guangzhou radar at certain times. The first cell appeared in Huadu district in Guangzhou at approximately 00:00:00 on May 7, 2017 (Fig. 3a), and then strengthened and maintained in the east of Huadu for a long time (Fig. 3b and Fig. 3c), contributing to the extraordinary rainfall observed there. At approximately 02:30:00, a small cell occurred in the region to the southeast of this Huadu cell (Fig. 3c). It developed and connected together with the aforementioned cell, and the regions with heavy precipitation maintained in the west of Zengcheng district (Fig. 3d and Fig. 3e). During this process, new cells appeared continuously in nearby areas, and experienced complicated merging and splitting processes among cells (Fig. 3c–e), while the system kept relatively steady in position with a slow southward movement. After approximately 07:00:00, some cells coming from the southwest side merged into the system, and the whole rainstorm system generally moved eastward, accompanied by complex generation and extinction processes of cells (Fig. 3f–h). The system clearly weakened and only sporadic lightning flashes could be observed after 12:00:00. According to the evolution of the rainstorm, the analysis period from 00:00:00 to 12:00:00 on May 7, 2017 was selected in this study. The primary precipitation cloud first occurring in the Huadu district was taken as the reference to select the analysis part of the rainstorm system. When the new cell merged into the part being focused on (their 30-dBZ echoes started to fuse), they became the analysis region from this moment. When one cell exceeding 30-dBZ echo was separated from the main convection body, it was excluded from the analysis. The concerned parts of the system were roughly indicated by the pink ellipses in Fig. 3. The lightning data used in the analysis were all within the selected regions. They were located within 100 km of the center of the LFEDA where the detection efficiency and accuracy of LFEDA was relatively high (Shi et al., 2017).

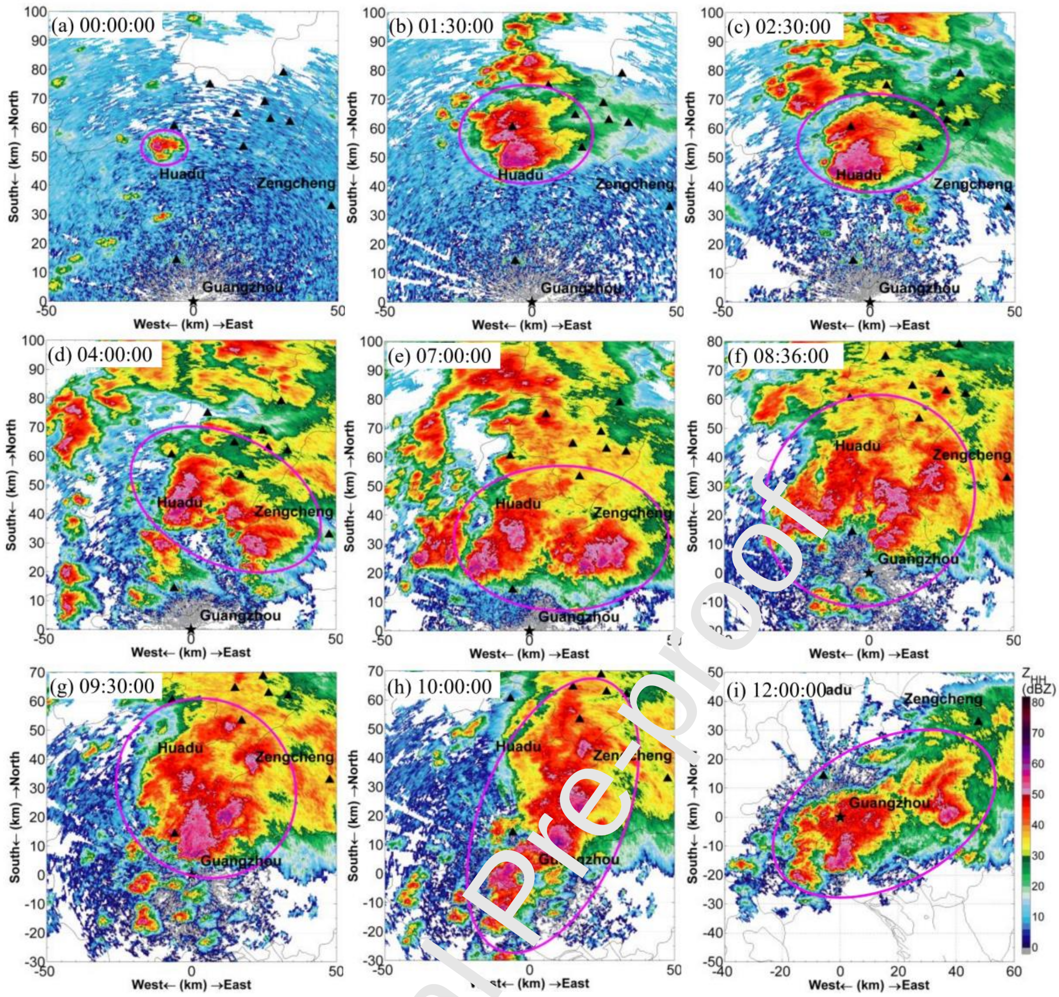

Fig. 3. Evolution of the rainstorm shown by the composite reflectivity of the Guangzhou radar. The pink ellipse area roughly surrounds the analyzed cells.

3. Overall lightning activity

According to the method described in section 2.1a, a total of 2072 flashes (CG flashes and IC flashes) were observed by the LFEDA during the analysis period and were derived from 44,439 selected LPDEs. The GDLLS located 563 CG flashes that will be referred to in following analysis. To understand the possible impact of detection efficiency of the LFEDA on the analysis, we investigated the ratios of CG flashes to total flashes and the average number of LPDEs per flash before and after 06:00:00, when the rainstorm was relatively close to, and away from, the center of the

LFEDA, respectively. The corresponding values were approximately 27% and 22 before 06:00:00 and 29% and 20 after 06:00:00, indicating that the detection efficiencies of the LFEDA for flash and LPDE should remain relatively steady during the analysis period.

Fig. 4 shows the changes in lightning activity and rainfall over time and the time-height distribution of the LPDEs. The information of initial position of 159 NILs selected according to the method introduced in section 2.1a is also exhibited in Fig. 4c and d, including 137 UNILs and 22 downward negative initial leaders (DNILs). As shown in Fig. 4a, the lightning was relatively active during the period from approximately 00:00:00 to 04:00:00, mainly corresponding to the cell above Huadu district (Fig. 3a–d), and then maintained low frequencies after 04:00:00. The lightning frequency hit a peak of 136 per 10 min from 01:30:00 to 01:40:00. The rainfall mass and maximum rate of rainfall in areas where the rainfall rate retrieved from the radar exceeded 2 mm h^{-1} are shown in Fig 4b. They were very different from the lightning rate in time changes. For example, after 04:00:00, the rate of lightning was much lower, but the rainfall mass was larger. Furthermore, the maximum rate of rainfall after 04:00:00 was generally analogous to that before 04:00:00.

The proportion of CG lightning to the total lightning was approximately 27%. The PCG lightning accounted for 10% of the total CG lightning, which was analogous to previous studies reporting the small proportion of PCG lightning in typical thunderstorms (Knupp, 2003; MacGorman et al., 1994; Zheng et al., 2010). However, it is interesting that the ratio of PCG lightning experienced a significant change during the evolution of the rainstorm. Before 04:00:00, the ratio of PCG lightning was only approximately 3%, and after 04:00:00 the value was approximately 24%. Fig. 4c indicates that the lightning discharges mainly occurred between the 0 and –40 °C environmental isotherms; this outcome was consistent with the main charging area suggested by the electrification mechanism (Pereyra et al., 2000; Takahashi, 1978) and the main temperature ranges of the lightning discharges reported in other types of thunderstorms (Krehbiel, 1986; Zheng et al., 2018, 2019a, b). The peak height of the LPDEs appeared at 6.3 km, corresponding to an environmental temperature of approximately –8 °C (Fig. 4d).

The height distribution of the NILs with different directions indicated the changing charge structures during the evolution of the rainstorm. According to Fig. 4c and d, before 04:00:00, the peak initiation height of the UNILs was 7.3 km, and that of the DNILs was 6.3 km, corresponding to approximately –15 and –8 °C environmental isotherms, respectively. Considering that the NIL developed from the edge of the negative charge core and toward the positive charge region, the above distribution suggested a macroscopic tripolar charge structure with an upper positive charge, middle negative charge and lower positive charge (Williams, 1989), where the main negative charge core was roughly located between –15 and –8 °C environmental isotherms. After 04:00:00, UNIL dominated the samples and their initiation heights decreased significantly, with the peak initiation height being 6.3 km (about environmental temperature of –8 °C). Tian et al. (2018) also reported that the precipitation cloud cluster during this period was a highly efficient tropical-type low-centroid precipitation cloud cluster. Therefore, this situation should correspond to a decrease in the main charge zone resulting from the weakened convection. The result suggested that the main negative charge core was below approximately –8 °C environmental temperature.

The changed charge structures and the height distributions of the charge regions might be responsible for the significant comparison of the ratio of PCG lightning before and after 04:00:00. In the case of the tripolar charge structure before 04:00:00, the CG lightning flashes were more likely contributed by the lower two charge regions (Proctor, 1991). Accompanied by the bidirectional propagations of the lightning leaders, the polarity of the CG lightning, i.e., the polarity of the downward grounding leader, is typically same as that of the upper charge region in these two charge levels (Zhang et al., 2006b). Therefore, under the situation of the normal tripolar charge structure, the NCG lightning was more likely to occur; therefore, PCG lightning only accounted for 3%. After 04:00:00, the weakening of convection led to a decrease in the rate of lightning. Meanwhile, the charge regions decreased in height, which was conducive to the discharge from the upper positive charge region towards the ground, resulting in a significant increase in the proportion of PCG lightning compared to the previous period (24% *versus* 3%).

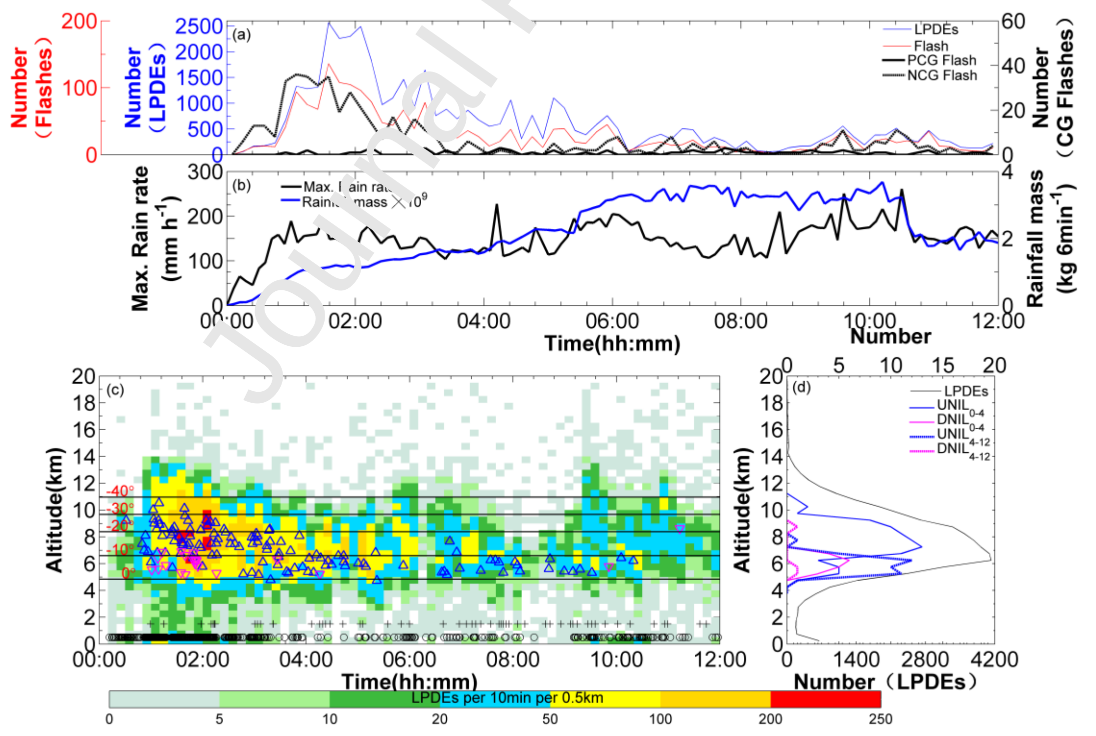

Fig. 4. Comprehensive lightning activity and rainfall from 00:00:00–12:00:00 on May 7, 2017. (a) Changes in the frequencies of lightning and LPDEs with time (10-min

interval). (b) Changes in the maximum rainfall rate and rainfall mass in the areas with rainfall rate above 2 mm h^{-1}, according to the rainfall rate retrieved from radar data. (c) Density of LPDEs as a function of height and time (shading colors; 10-min interval and 0.5-km span). The initiation of UNILs (indicated by blue triangles) and DNILs (indicated by pink inverted triangles) and the PCG lightning flashes (black "+") and NCG lightning flashes (black "○") are superposed. The solid white lines indicate the height of the 0, –10, –20, –30, and –40 °C environmental isotherms, which were provided by the Qingyuan sounding at 20:00:00 on 6 May 2017. (d) Height distributions of LPDEs (black solid line), UNILs (black lines) and DNILs (pink lines). The blue and pink solid lines are associated with the samples between 00:00:00 and 04:00:00. The blue and pink dotted lines are associated with the samples between 04:00:00 and 12:00:00.

4. Association of lightning activity with cloud structures

4.1. Spatial correspondence between lightning and precipitation

During the analysis, we found that the areas with active lightning discharges did not correspond to the heavy precipitation center. Fig. 5 shows the surface rainfall rate and superposed LPDEs and flash initiations at certain times. The heavy precipitation cores in Fig. 5a and b are mainly associated with the cells in Huadu district, and those in Fig. 5c and d are mainly associated with the cells in Zengcheng district. We can find that the positions of lightning discharges and initiations significantly deviated from the heaviest precipitation zone in space. The LPDEs and flash initiations predominantly occurred in the areas where the precipitation was less than 20 mm h^{-1}. This situation was common in different cells of the rainstorm.

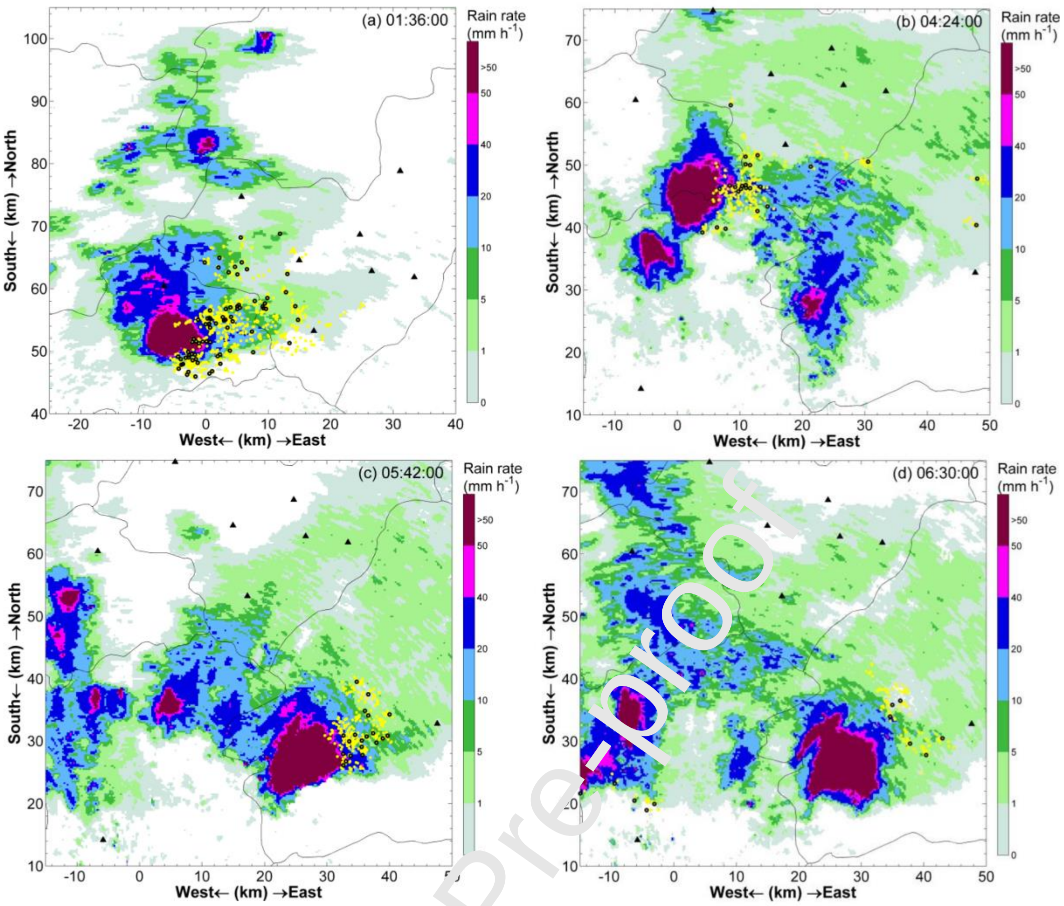

Fig. 5. LPDEs and flash initiations superposed on the rainfall rate retrieved from the radar data during the radar volume scans starting at approximately 01:36:00 (a), 04:24:00 (b), 05:42:00 (c) and 06:30:00 (d) on May 7, 2017. The chosen LPDEs (yellow dots) and flash initiations (black hollow dots) were within the 6-min radar volume scan period.

Fig. 6 shows the resulted spatial distribution of the LPDEs and flash initiations in the rainstorm during the whole analysis period while the accumulated rainfall retrieved from the radar are superposed. There were two areas with high densities of LPDEs and flash initiations indicated by the contours in the horizontal patterns (Fig. 6c1 and c2). They were generally associated the cells responsible for the heaviest precipitations. But, it was worth noting that the areas with the heaviest precipitation were spatially separated from the positions with the large-density cores of LPDEs and flash initiations. The spatial separation was more apparent in the areas related to the east heavy precipitation core occurring in Zengcheng district.

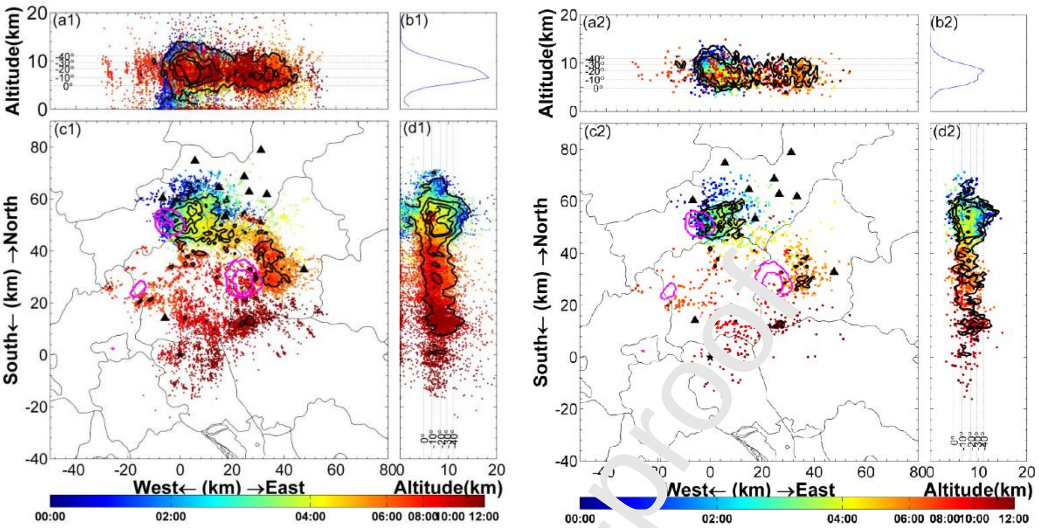

Fig. 6. Spatial distribution of LPDEs (a1–d1) and flash initiations (a2–d2) in the rainstorm from 00:00:00–12:00:00 on May 7, 2017. The colors of the dots ranging from blue to red indicate the times of the LPDEs or flash initiations. The black contours indicate the density of LPDEs or flash initiations (statistical grid is 1 km). They represent 20, 100, 200, and 300 per square kilometer from the outside to the inside for the LPDEs; while the corresponding values are 2, 5 and 10 per square kilometer for the flash initiations. The pink contours indicate the rainfall retrieved from the radar data during the analysis period, the relevant values are 150 and 250 mm from the outside to the inside. The 0, –10, –20, –30, and –40 °C environmental isotherms are labeled in a and b, similar to those in Fig. 4c.

In Fig. 7, we show the probability distributions of the LPDEs and flash initiations corresponding to the rate of surface rainfall. Both the probability distributions of the LPDEs and flash initiations followed lognormal distributions, concentrating numerous samples in weak-precipitation intervals, with a long tail toward heavy precipitation. Approximately 51% of LPDEs and 47% of flash initiations occurred in areas where the rate of rainfall was less than 10 mm h^{-1}, while the maximum rate of rainfall nearly always exceeded 100 mm h^{-1} (Fig. 4b). Approximately 72% of the LPDEs and 67% of flash initiations corresponded to rates of rainfall below 20 mm h^{-1}. In contrast, LPDEs and flash initiations occurring in areas with a precipitation intensity exceeding 40 mm h^{-1} only accounted for approximately 12% and 14%, respectively. In the case where most of flash initiations and LPDEs preferred to correspond to a low rate of rainfall, flash initiations exhibited a slightly higher probability of occurring over areas with a higher rate of rainfall than the LPDEs. Because of the observed change in the flash rate (Fig. 4a), we further compared the distributions of LPDEs and flash initiations as a function of the rate of surface rainfall before and after 04:00:00 (data not shown). Before 04:00:00, the LPDEs corresponding to rainfall rates lower than 10 mm h^{-1}, lower than 20 mm h^{-1}, and higher than 40 mm h^{-1}, accounted for approximately 49%, 70%, and 13%, respectively. The corresponding values for flash initiations were approximately 44%, 64%, and 17%, respectively. After 04:00:00, the relevant ratios were 54%, 74%, and 10% for LPDEs and 52%, 70%, and 11% for flash initiations, respectively. These results further suggest that lightning activity predominantly occurred over areas featuring relatively low precipitation, and that these were usually in different cells and stages of development of the rainstorm.

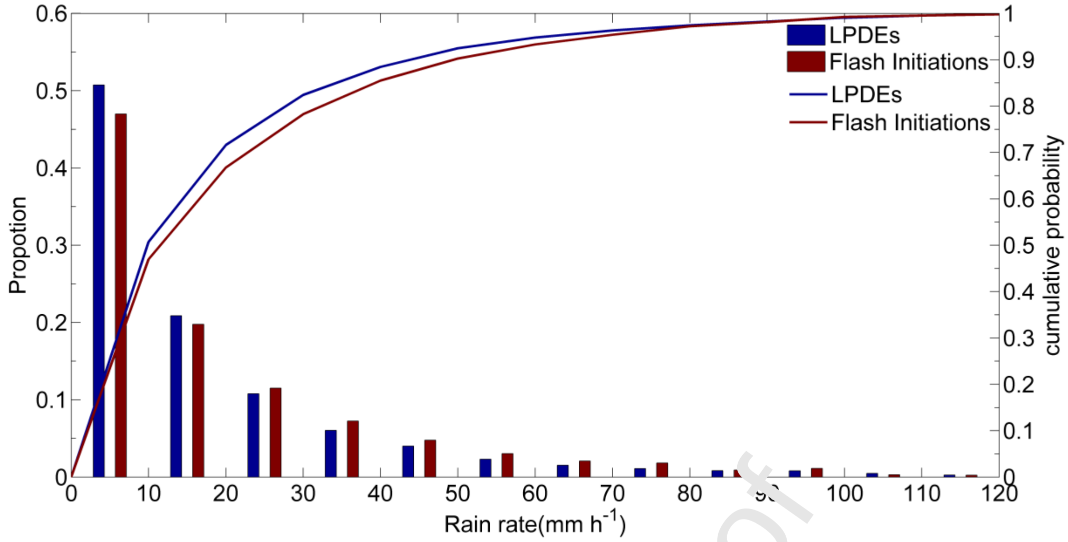

Fig. 7. Distributions of LPDEs and flash initiations corresponding to different rainfall rates.

Considering the correspondence of lightning activities to the rainfall rate, in the following analysis of sections 4.2 and 4.3, the samples will be divided into three regions according to the surface rainfall rate as follows: rainfall rate less than or equal to 10 mm h^{-1} ($R_{\leq 10}$), greater than 10 mm h^{-1} and less than 40 mm h^{-1} ($R_{10\text{–}40}$) and greater than or equal to 40 mm h^{-1} ($R_{\geq 40}$), aiming to compare their differences.

4.2. Hydrometeors associated with lightning discharges

Considering that the vertical spatial resolution in the distance far from the radar is low and the cone of silence near to radar, we only chose LPDEs and flash initiations within 1 km above or below each radar scanning cone in this analysis. Additionally, since the step or dart leader of the CG flash did not propagate through the charge region after it developed out of the cloud, we excluded the LPDEs below 3 km. Regardless of whether a radar grid box had only one LPDE (flash initiation) or multiple LPDEs (flash initiations), the attribute of hydrometeors in the grid box was only counted once. The statistics were performed based on a radar volume scan lasting 6 minutes. With the data control, the sample numbers of the grid boxes with LPDEs in the $R_{\leq 10}$, R_{10-40}, and $R_{\geq 40}$ regions were 9713, 6192 and 1653, respectively. The corresponding sample numbers of the grid boxes with flash initiations were 590, 422 and 176, respectively.

Fig. 8 shows the vertical distributions of the relative proportion of grid boxes dominated by different-type hydrometeors associated with the LPDEs (Fig. 8a–c) and flash initiations (Fig. 8d–f) at 1-km height intervals. The proportion values of the four main hydrometeors associated with the LPDEs and flash initiations during the evolution of the rainstorm are shown in Table 1 and 2, respectively. It is revealed that the positions with LPDEs and flash initiations were mainly dominated dry aggregated snow.

During the whole analysis period, the grid boxes dominated by dry aggregated snow and with LPDEs (flash initiations) accounted for approximately 81% (87%) of all the grid boxes with LPDEs (flash initiations); for the grid boxes dominated by graupel and with LPDEs (flash initiations), the ratio was about only 9% (8%). In the three investigated regions including $R_{\leq 10}$, R_{10-40}, and $R_{\geq 40}$ (Fig. 8 and Tables 1 and 2), the grid boxes featuring dry aggregated snow and with LPDEs (flash initiations) also occupied the largest proportion, with the corresponding proportion values being 84% (91%), 79% (84%) and 71% (81%), respectively; the counterparts for the graupel grid boxes with LPDEs (flashes) were 3% (3%), 13% (11%) and 22% (16%), respectively. These results showed that the proportion of graupel grid boxes with LPDEs and flash initiations increased as one moved toward the strong precipitation area. For example, in the $R_{\geq 40}$ region, the proportion of graupel grid boxes with LPDEs (flash initiations) to all grid boxes with LPDEs (flash initiations) was approximately 7 (5) times that in the $R_{\leq 10}$ region. Meanwhile, if the hydrometeors between 5 and 7 km (approximately between –1.1 and –12.6 ℃ environmental isotherms) were checked specifically, the proportions of graupel grid boxes with LPDEs (flash initiations) in the $R_{\leq 10}$, $R_{10–40}$, and $R_{\geq 40}$ regions were 5% (4%), 25% (22%), and 64% (66%), respectively, indicating that the lightning discharges between 5 and 7 km in the regions with rainfall rate below 40 mm h^{-1} were still mainly related to the charged dry aggregated snow, but those at 5–7 km over the $R_{\geq 40}$ region were mainly related to charged graupel. Checking the height distributions of the lightning discharges and flash initiations (black lines in Fig. 8), we found that the LPDEs (flash initiations) in the $R_{\leq 10}$, $R_{10–40}$, and $R_{\geq 40}$ regions peaked at 6.5 (5.5), 6.5 (8.5), and 8.5 (9.5) km, respectively, and the predominant particles at the peak heights were all dry aggregated snow. For the $R_{10–40}$, and $R_{\geq 40}$ regions, there were second peaks of LPDEs (flash initiations) at 8.5 (5.5) and 6.5 (6.5) km, respectively. For the $R_{\geq 40}$ region, the secondary peak heights corresponded to more graupel grid boxes with LPDEs and flash initiations. The above characteristics also indicated that the regions with greater rainfall rate featured stronger convection than the regions with smaller rainfall rate, which supported the generation of more graupel and the flash initiations and discharges to occur at higher positions.

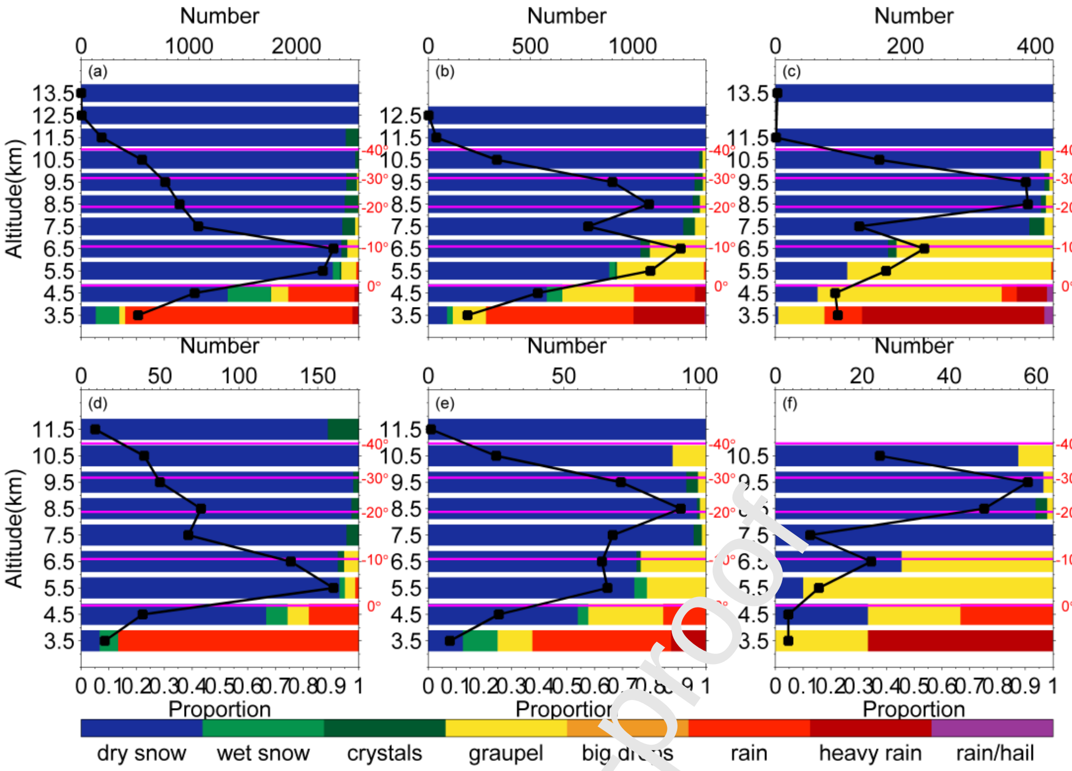

Fig. 8. The height distributions of the radar grid boxes with different-type dominant hydrometeors associated with LPDEs (a – c) and flash initiations (d – f). a and d: The region where the rainfall rate is less than or equal to 10 mm h^{-1} ($R_{\leq 10}$). b and e: The region where the rainfall rate is between 10 mm h^{-1} and 40 mm h^{-1} (R_{10-40}). c and f: The region where the rainfall rate was greater than or equal to 40 mm h^{-1} ($R_{\geq 40}$). The statistical height interval is 1 km. The relative proportions of the grid boxes with different-type hydrometeors associated with LPDEs are counted at each height interval. The solid red lines marked the 0, –10, –20, –30, and –40 °C environmental isotherms, similar to those in Fig. 4c.

Table 1. The proportions of radar grid boxes with some main hydrometeors associated with LPDEs to all radar grid boxes with LPDEs.

Hydrometeors	$R_{\leq 10}$	R_{10-40}	$R_{\geq 40}$
Dry aggregated snow	84%	79%	71%

Graupel	3%	13%	22%
Light and moderate rain	7%	4%	1%
Crystals of various orientations	2%	2%	2%

Table 2. The proportions of radar grid boxes with some main hydrometeors associated with flash initiations to all radar grid boxes with flash initiations.

Hydrometeors	$\mathbf{R_{\leq 10}}$	$\mathbf{R_{10\text{–}40}}$	$\mathbf{R_{\geq 40}}$
Dry aggregated snow	91%	84%	81%
Graupel	3%	11%	16%
Light and moderate rain	4%	2%	1%
Crystals of various orientations	2%	2%	1%

4.3 Vertical airflow associated with lightning discharges and flash initiations

In this section, we focus on the vertical airflow in radar grid boxes containing LPDEs and flash initiations. One radar grid box with any number of LPDEs or flash initiations was counted only once. The distributions of the LPDEs and flash initiations in the $R_{\leq 10}$, $R_{10\text{–}40}$, and $R_{\geq 40}$ regions as a function of the velocity of vertical airflow are shown in Fig. 9, where upward (downward) velocities are positive (negative). The LPDEs and flash initiations were strongly associated with locations characterized by weak updrafts and downdrafts. For example, there were approximately 56% (47%) of LPDEs (flash initiations) in the interval of vertical airflow velocity between −2 and 2 m s^{-1}. In the interval of vertical airflow velocity ranging from −4 to 4 m s^{-1}, the corresponding ratios were 74% for LPDEs and 68% for flash initiations. In the $R_{\leq 10}$, $R_{10\text{–}40}$, and $R_{\geq 40}$ regions, the ratios of LPDEs (flash initiations) corresponding to the vertical airflow velocity interval from −2 to 2 m s^{-1} were 65% (59%), 44% (37%), and 38% (22%), respectively. The ratios of LPDEs (flash initiations) corresponding to the interval from −4 to 4 m s^{-1} were 83% (79%), 63% (58%), and 57% (44%), respectively. These results indicated that the lower the rate of rainfall, the higher the proportions of LPDEs and flash initiations appearing in regions with weak updrafts and downdrafts. This might also be a manifestation of the overall weaker convection in regions with low precipitation intensities.

Generally, lightning discharges were slightly more likely to occur in regions with updrafts than those with downdrafts. Approximately 58% (59%) of the grid boxes with LPDEs (flash initiations) featured updrafts. But, in regions with high rates of rainfall, LPDEs (flash initiations) tended to have a larger proportion of samples in intervals with large downdrafts than in intervals with large updrafts. For example, in the $R_{\geq 40}$ region, grid boxes with LPDEs (flash initiations) and featuring a downward airflow velocity less than 4 m s^{-1} (a relatively strong downdraft), accounted for approximately 26% (39%), while those associated with an upward vertical airflow velocity exceeding 4 m s^{-1} (a relatively strong updraft), accounted for 16% (17%). In contrast, the corresponding values in the $R_{\leq 10}$ region were 6% (10%) and 10% (11%), for downdrafts and updrafts, respectively. These results should be associated with the relatively stronger updrafts and downdrafts in regions with heavier precipitation.

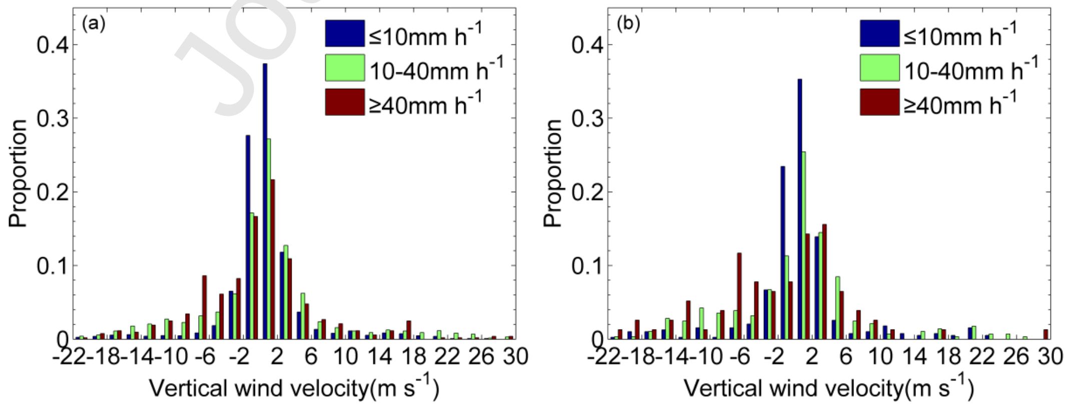

Fig. 9. Distributions of the radar grid boxes with LPDEs (a) and flash initiations (b) corresponding to vertical airflow velocity.

5. Discussions

Previous studies on the mechanisms of the triggering, organization, and maintenance, and precipitation characteristics of this rainstorm have demonstrated that it was a high-efficiency precipitation system dominated by warm cloud precipitation, with weak convection and a high ratio of small-size raindrops in the raindrop spectrum (Fu et al., 2018; Tian et al., 2018; Xu et al., 2018; Zeng et al., 2018; Zhang et al., 2019; Zhang et al., 2018). We further examined the vertical development of this rainstorm by plotting the vertical cross sections of reflectivity and differential reflectivity (Fig. 10), where the flash initiations and LPDEs are also presented. Strong radar echoes mainly occurred at lower heights. For example, the 40-dBZ echo top barely exceeded the −10 °C environmental isotherm (approximately 6.6 km). In contrast, Liu et al. (2011) demonstrated that the 40-dBZ echo top developed through 10 km in a mesoscale convective system over Beijing, while Zhang et al. (2017) observed a 40-dBZ echo top above 12 km in a supercell. Some studies suggested that the 40-dBZ echo top must exceed 7 km or −10 °C environmental isotherm for lightning to occur (Martinez, 2002; Vincent et al., 2003; Wang et al., 2008). Thus, the current rainstorm barely exceeded the critical condition that could cause lightning to occur. Furthermore, we determined the distributions of reflectivity at locations associated with flash initiations and LPDEs, and found that they followed the normal distribution pattern, with a peak between 24 and 28 dBZ (Fig. 11). The mean and median reflectivity values associated with flash initiations were approximately 27 dBZ each and the corresponding values for the LPDEs were approximately 26 dBZ each. In an investigation of the radar signals associated with lightning in the summer of 2017 in northeastern Switzerland, Ventura et al. (2019) reported that most flashes originated in areas with a reflectivity of approximately 40 dBZ, and they also mainly propagated within such regions. In a study involving multicells, mesoscale convective systems, and supercells, Mecikalski and Carey (2018) documented that the peaks of the distributions of reflectivity associated with flash initiations were between 30 – 35 dBZ, 30 – 35 dBZ, and 35 – 40 dBZ, respectively. The above analysis and comparisons further indicate that the rainstorm examined in the present study was characterized by weak convection. The weak convection caused weak ice-phase growth and a weak charging process, and consequently the generally infrequent lightning activity.

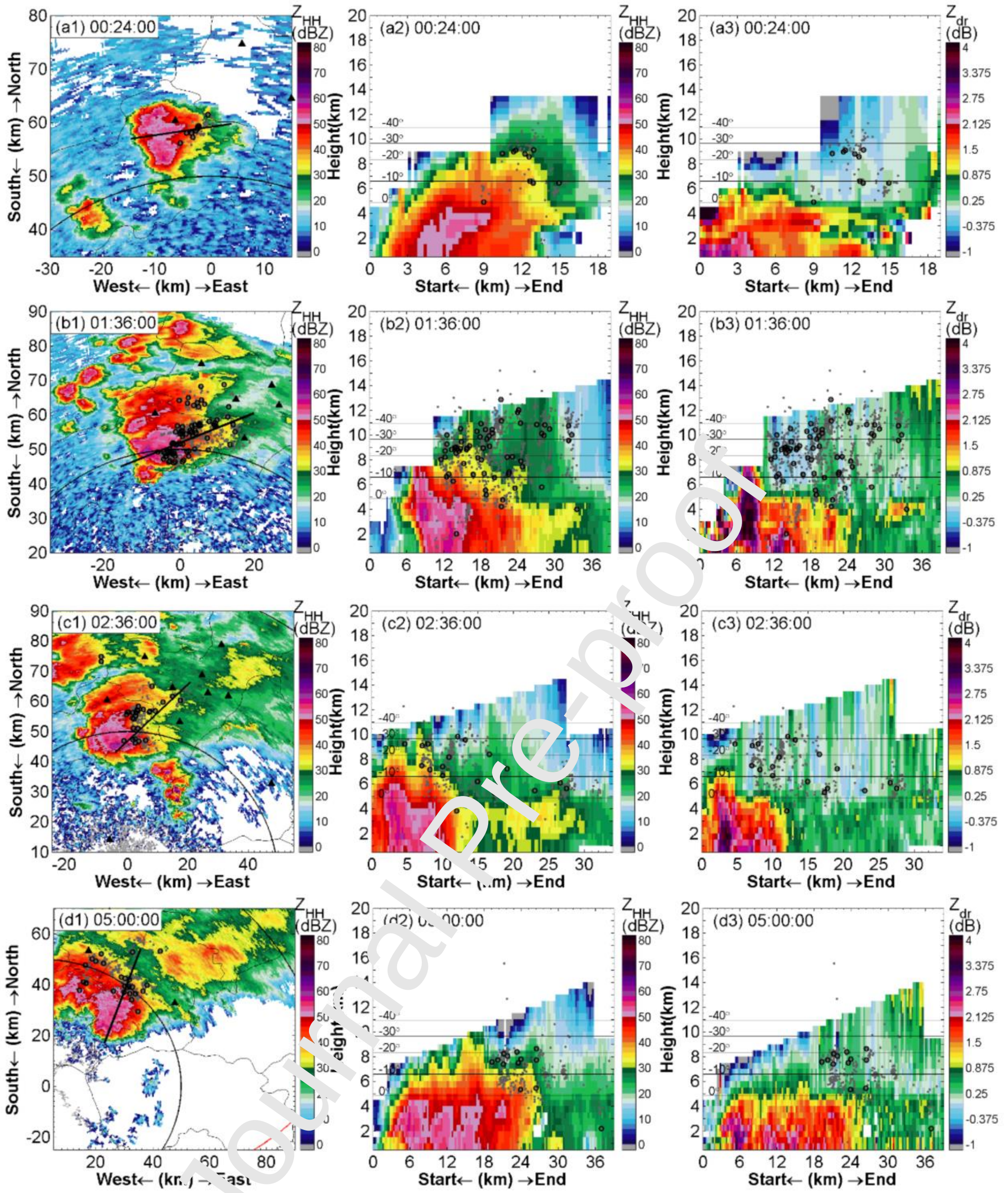

Fig. 10. Vertical cross sections of radar reflectivity and differential reflectivity (Z_{dr}) at 00:24:00 (a2 – a3), 01:36:00 (b2 – b3), 02:36:00 (c2 – c3), and 05:00:00 (d2 – d3). The positions of the vertical cross sections are indicated by the black lines superposed over the radar composite reflectivity in a1, b1, c1, and d1. The flash initiations are marked by hollow black circles, and LPDEs are marked by gray dots. In the vertical cross sections, the flash initiations and LPDEs within 5 km of the vertical cross sections are superposed. The 0, −10, −20, −30, and −40 °C environmental isotherms are similar to those in Fig. 4c.

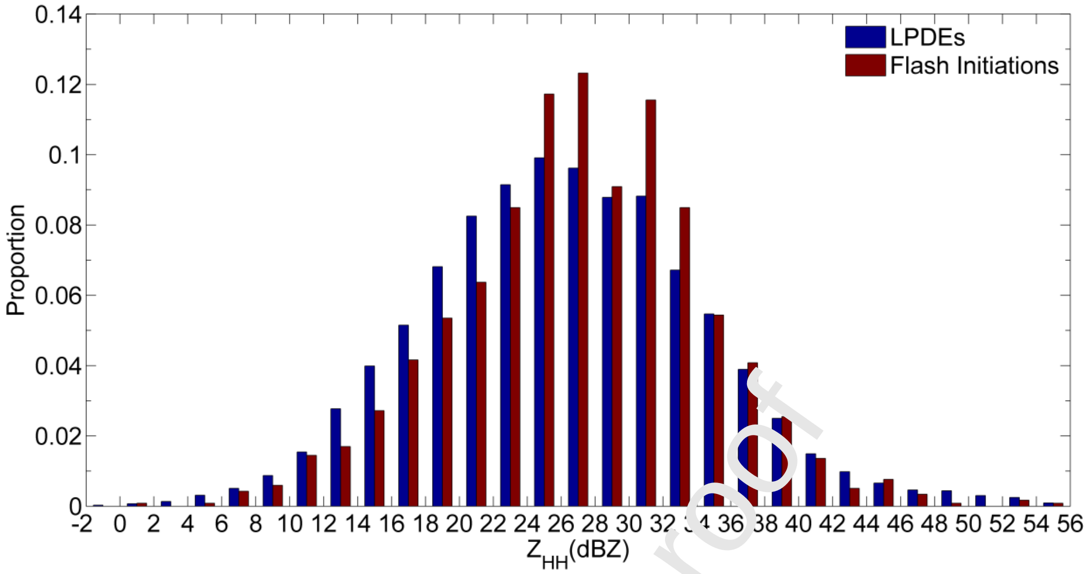

Fig. 11. Distributions of reflectivity at positions with flash initiations and LPDEs.

The results presented in section 4 suggest that convection should be relatively stronger in areas with relatively heavy precipitation compared to areas with relatively weak precipitation. For example, there was a higher ratio of larger ice particles (i.e., graupel) associated with lightning discharges in the $R_{\geq 40}$ region than in the $R_{\leq 10}$ and $R_{10–40}$ regions. The $R_{\geq 40}$ region was dominated by graupel particles associated with lightning discharges between 5 and 7 km, while all levels above the 0 °C environmental isotherm in $R_{\leq 10}$ and $R_{10–40}$ regions were entirely dominated by dry aggregated snow. According to Fig. 10, above the regions of heavy precipitation (indicated by the large reflectivity and differential reflectivity at lower level), there were higher top of strong echo (e.g., 40 dBZ), and large value of differential reflectivity (e.g., 1 dB) tended to have relatively larger vertical extension. Occasionally, differential reflectivity columns, the signal of convection (Kumjian et al., 2014), were apparent. Therefore, it is concluded that the generation and growth of ice-phase particles should mainly occur in regions associated with heavy precipitation (although a large number of rain drops did not experience the ice-phase process before they fell, contributing to the warm cloud precipitation). According to the universally accepted non-inductive electrification mechanism (Pereyra et al., 2000; Takahashi, 1978), graupel and ice crystals are the main particles participating in the charging process. Therefore, it is concluded that the main charging process should occur in regions associated with heavy precipitation, where relatively stronger convection and relatively more graupels existed. Some small charged ice-phase particles were brought to the upper level by the weak updraft and brought to the periphery of the heavy precipitation region by advection, where they should be related to lightning discharges.

It seems that regions with the main lightning discharges were spatially separated from regions that mainly contributed to the charging process. While the main charging processes were associated with heavy precipitation, the flash initiations and LPDEs over the $R_{\geq 40}$ region only accounted for approximately 14% and 12% of all the samples, respectively. Many flash initiations and LPDEs occurred in the regions horizontally away from the convection regions (Fig. 10). Graupel predominately associated with lightning discharges over the $R_{\geq 40}$ region was located between approximately 5 and 7 km or between −1.1 and −12.6 °C environmental isotherms (Fig. 8c, f), suggesting that the main charging process might occur around −10 °C environmental isotherm. Meanwhile, the most active lighting discharges over the $R_{\geq 40}$

region occurred at a height of approximately 9 km (Fig. 8), suggesting a vertical separation of charging and discharging locations. This is why lightning discharges were significantly spatially associated with dry aggregated snow (relatively small particles). The relatively large ice-phase particles might directly fall in the heavy precipitation core or fall earlier during their transportation because of the weak convection and relatively large mass of these particles.

We attempt to give a explanation with the conceptual sketch map of Fig. 12. Fig. 12a shows the situation of this rainstorm with weak convection and dominated by warm precipitation process, and Fig. 12b shows the possible situation in a thunderstorm with strong convection as a comparison.

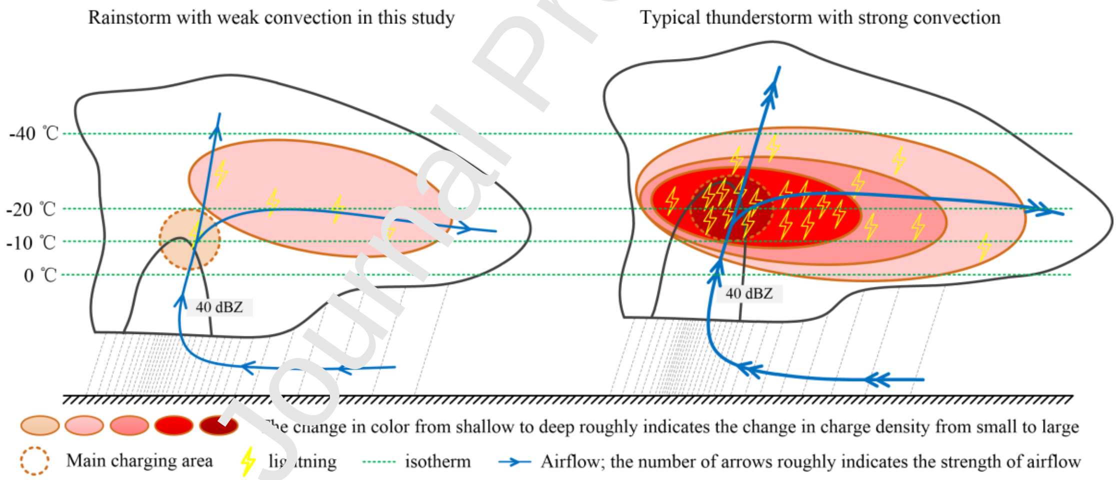

Fig. 12. Conceptual sketch map showing the spatial relationship of lightning discharge regions with the main charging regions in the rainstorm with (a) weak convection, as observed in this study; and (b) a typical thunderstorm with strong convection.

To generate a lightning discharge, it is necessary for the charge density to reach a certain level to generate an electric field sufficiently strong to cause a discharge.

Under conditions of overall weak convection in this rainstorm (Fig. 12a), the charging process, which is believed to have mainly occurred in the region with relatively strong convection and heavy precipitation, was inefficient and slow. Furthermore, weak updraft and advection transported small charged particles upwards and downwind, and large charged particles fell quickly. The inefficient and slow charging process, coupled to the transfer of charge from their area of origin, was not conducive to the aggregation of sufficient charge. Therefore, it might be difficult to form continuous regions with a sufficiently high charge density for lightning discharge to occur in the charging region. In contrast, in regions away from and above the main charging region, the transported charged small ice-phase particles could stably exist for a long time under weak airflow, which was favorable to the aggregation of sufficient charge and a high charge density in local area, thereby supporting the occurrence of lightning discharges.

The analysis about this rainstorm and some previous studies provide support for the above speculation. In Fig. 9 and the relevant analysis, we have noted that most of the lightning discharges occurred in the regions with weak updraft and downdraft. Based on the numerical model study, Wang et al. (2015) indicated that ice particles in regions with a vertical velocity between 1 and 5 m s^{-1} acquired the most charge during the lifetime of the thunderstorm. They suggested that the quasi-steady regions featuring a vertical velocity ranging from –1 to 1 m s^{-1} were the most beneficial to the separation of different-polarity charges. Meanwhile, the charges were mainly contributed by the regions with relatively strong updrafts. Xu et al. (2016) noted the function of the aggregation of charge particles in enhancing the lightning activity. In one hailstorm investigated by them, there were two stages featuring high-rate lightning flashes; the first was around the hailfall time and the second was after the end of the hail and during the period when the convection of the storm continuously weakened. It is surprising that the lightning frequency in the second stage had a significantly larger peak than that in the first stage. They speculated that after the strong downdrafts accompanying the hailfall suddenly ended, the airflow in the storm weakened and provided conditions for small-size charged particles to aggregate in the middle and lower levels (a low lightning discharge height was observed), causing high-density charge regions and even more active lightning discharges.

In a thunderstorm featuring strong convection, circumstances may differ (Fig. 12b). The main charging process occurs in a region with strong convection. Although charged particles are also transported outwards, strong convection supports a more efficient charging process and a high charge density is therefore maintained in the charging region. However, because of the sedimentation and diffusion of charged particles during their transport outwards, charge density tends to decrease with distance travelled, making lightning activity generally more frequent in and around the charging regions, and weakening in regions away from the charging regions. This is why, in typical or severe thunderstorms, the active lightning discharges were usually observed in regions with strong convection, shear, or turbulence (Bruning and MacGorman, 2013; Carey, et al., 2005; Feng et al., 2007; Liu et a., 2001; López et al., 1990; Ribaud et al., 2016; Zhang et al., 2017; Zheng and MacGorman, 2016; Zheng et al., 2010).

In summary, in circumstances similar to those represented in Figure 12a and b, the essential difference among them is the relationship between the rate of charging and the speed of charge transfer from the area of origin. If the former is slower than the latter, the lightning flashes in the region in or near to the area of origin of charging may be relatively infrequent, and the aggregation of charges in the region away from the area of origin of charging may cause relatively frequent lightning flashes. This situation should occur in storms with weak convection. In contrast, if the former is faster than the latter, the area of origin of charging should have the highest charge density and therefore features the most frequent lightning discharges. Furthermore, the charge density generally decreases with distance from the area of origin of charging, causing a decreasing frequency of lightning flashes with increasing distance. This situation should occur in storms with strong convection.

Strong convective thunderstorms also tend to have more abundant large particles associated with the charging process and lightning discharges. For example, in an analysis of a supercell cluster, Zheng and MacGorman (2016) reported that the flash initiation points located in positions dominated by graupel and dry aggregated snow accounted for 44.3% and 44.1% of the total flash initiation points, respectively. Applying the same method as used in the present study, we recalculated the supercell cluster of Zheng and MacGorman (2016) and found that grid boxes with flash initiations and dominated by graupel and dry aggregated snow accounted for approximately 49% and 39%, respectively, of total grid boxes, and the corresponding values for flash sources (roughly similar to the LPDEs used in the present study) were 43% and 38%, respectively, indicating a stronger association of lightning discharges with graupel. In a study of a bow-echo system, Ribaud et al. (2016) reported that the percentages of graupel areas with flash initiations and propagations were approximately 70% and 58%, respectively, which is also significantly different from the results of the present study.

6. Conclusions

In this study, 3-D lightning location data and polarimetric radar data were mainly used to analyze lightning activities and their associations with cloud structures in a rainstorm featuring weak convection and predominated by warm cloud precipitation in Guangzhou on May 7, 2017, and the following conclusions were obtained:

The lightning discharges were mainly concentrated in the height range from approximately 4–12 km, corresponding to an environmental temperature layers from approximately 0 to –40 °C, and a peak height of 6.3 km, corresponding to about –8 °C environmental temperature. There were 2072 detected LFEDA lightning flashes, of which the CG lightning flashes accounted for approximately 27%. The ratio of PCG lightning to CG lightning was approximately 10% during the analysis period from 00:00:00 to 12:00:00, while it was only approximately 3% before 04:00:00 and reached up to approximately 24% after 04:00:00.

Before approximately 04:00:00, there was generally a typical tripolar charge structure with an upper positive charge, middle negative charge and lower positive charge, the negative charge core being between approximately –15 and –8 °C environmental isotherms; after that time, the main charge regions significantly reduced in height, accompanied by further weakened convection, with the negative charge core deduced to be below approximately –8 °C environmental isotherm. The changing charge structures might be responsible for the distinct ratios of PCG lightning during the two periods.

The lightning discharges predominantly occurred in regions corresponding to relatively weak precipitation intensity and convection, causing the significant spatial separation between active lightning discharging and heavy precipitation core. The LPDEs (flash initiations) located in the $R_{\leq 10}$ and $R_{\geq 40}$ regions accounted for approximately 51% (47%) and 12% (14%), respectively.

The predominant hydrometeor associated with lightning discharges was dry aggregated snow. Overall, approximately 81% (87%) of radar grid boxes with LPDEs (flash initiations) were dominated by dry aggregated snow, and only 9% (8%) of the radar grid boxes with LPDEs (flash initiations) were dominated by graupel. Only between 5 and 7 km over the $R_{\geq 40}$ region, the areas with lightning discharges were dominated by graupel, with the corresponding ratios being 64% for LPDEs and 66% for flash initiations.

Most of the flash discharges were distributed in locations featuring weak updrafts and downdrafts. Approximately 74% of LPDEs and 68% of flash initiations were concentrated in the range of vertical airflow velocity between −4 and 4 m s^{-1}.

It is speculated that the weak convection of this rainstorm made charging inefficient and slow. Furthermore, small charged ice-phase particles were transported upwards and outwards as a result of weak updraft, and advection, respectively. These conditions were not conducive to the formation of a high charge density in the area of origin of charging. The effective aggregation of the small charged particles in local areas away from the area of origin of charging and with relatively steady airflow supported the development of a sufficiently higher charge density for the occurrence of lightning discharge. Consequently, more lightning flashes were observed in regions dominated by dry aggregated snow (relatively small particles) and correspondingly weak precipitation. The circumstances in this rainstorm may be different from those in a typical thunderstorm with strong convection and an efficient and fast charging process. This in turn makes the charge density in the area of origin of charging bigger than in other regions, resulting in the most active lightning discharge in and around the area of origin of charging.

Acknowledgements

This work was supported by the National Key Research and Development Program of China (2017YFC1501503), National Natural Science Foundation of China (41675005 and 41975003), and Basic Research Fund of CAMS (2020Z009). The data associated with this paper can be accessed from http://doi.org/10.5281/zenodo.3902180 or from the corresponding author.

References:

Bitzer, P.M., Christian, H.J., Stewart, M., Burchfield, J., Podgorny, S., Corredor, D., Hall, J., Kuznetsov, E., Franklin, V., 2013. Characterization and applications of VLF/LF source locations from lightning using the Huntsville Alabama Marx Meter Array. J. Geophys. Res. Atmos. 118(8), 3120–3138. https://doi.org/10.1002/jgrd.50271.

Bruning, E.C., MacGorman, D.R., 2013. Theory and observations of controls on lightning flash size spectra. J. Atmos. Sci. 70(12), 4012 – 4029. https://doi.org/10.1175/JAS–D–12–0289.1.

Carey, L. D., Murphy, M. J., McCormick, T. L., Demetriades, N. W. S., 2005. Lightning location relative to storm structure in a leading-line, trailing-stratiform mesoscale convective system. J. Geophys. Res. Atmos., 110 (D3), D03105, https://doi.org/10.1029/2003JD004371.

Chen, H., Chandrasekar, V., Bechini, R., 2017. An improved dual-polarization radar rainfall algorithm (DROPS2. 0): Application in NASA IFloodS field campaign. J. Hydrometeorol, 18(4), 917–937. https://doi.org/10.1175/JHM–D–16–0124.1.

Chen, L., Zhang, Y., Lu, W., Zheng, D., Zhang, Y., Chen, S., Huang, Z., 2012. Performance evaluation for a lightning location system based on observations of artificially triggered lightning and natural lightning flashes. J. Atmos. Ocean Tech. 29(12), 1835–1844. https://doi.org/10.1175/JTECH–D–12–00028.1.

Chen, Z., Zhang, Y., Zheng, D., Zhang, Y., Fan, X., Fan, Y., Xu, L., Lyu, W., 2019. A method of three-dimensional location for LFEDA combining the time of arrival method and the time reversal technique. J. Geophys Res: Atmos. https://doi.org/10.1029/2019JD030401.

Coleman, L.M., Marshall, T.C., Stolzenburg, M., Hamlin, T., Krehbiel, P.R., Rison, W., Thomas, R.J., 2003. Effects of charge and electrostatic potential on lightning propagation. J. Geophys. Res. Atmos. 108(D9). https://doi.org/10.1029/2002JD002718.

Cummins, K. L., M. J. Murphy, E. A. Bardo, W. L. Hiscox, R. B. Pyle, and A. E. Pifer, 1998: A combined TOA/MDF technology upgrade of the U.S. National Lightning Detection Network. J. Geophys. Res., 103, 9035–9044, https://doi.org/10.1029/98JD00153.

Fan, X.P., Zhang, Y.J., Zheng, D., Zhang, Y., Lyu, W.T., Liu, H.Y., Xu, L.T., 2018. A new method of three-dimensional location for Low-frequency Electric Field Detection Array. J. Geophys. Res: Atmos. 123(16), 8792 – 8812. https://doi.org/10.1029/2017JD028249.

Feng, G., Qie, X., Yuan, T., Niu, S., 2007. Lightning activity and precipitation structure of hailstorms. Sci. China Ser. D-Earth Sci. 50(4), 629y an. https://doi.org/10.1360/yd2007-50-4-629.

Fu, P., Hu, D., Zhang, Y., Li, H., Gao, M., Zhou, X., 2018. Microphysical characteristics, initiation and maintenance of record heavy rainfall over

Guangzhou region on 7 May 2017. Meteor. Mon. 44 (4), 500–510. https://doi.org/10.7519/j.issn.1000–0526.2018.04.003.(In Chinese)

Knupp, K. R., Paech, S., Goodman, S., 2003. Variations in cloud-to-ground lightning characteristics among three adjacent tornadic supercell storms over the Tennessee Valley region. Mon. Weather. Rev. 131(1), 172 – 188. https://doi.org/10.1175/1520–0493(2003)131<0172:VICTGL>2.0.CO;2.

Krehbiel, P. R. (1986). The electrical structure of thunderstorms. Chapter 8 of The Earth's electrical environment (pp. 900The E Washington,DC: The National Academies Press. https://doi.org/10.17226/898.

Kumjian, M.R., Khain, A.P., Benmoshe, N., Ilotoviz, E., Ryzhkov, A.V., Phillips, V.T., 2014. The anatomy and physics of ZDR columns: Investigating a polarimetric radar signature with a spectral bin microphysical model. J. Appl. Meteor. Climatol. 53, 1820053, 18https://doi.org/10.1175/JAMCorg/20ith a .

Liu, D., Qie, X., Xiong, Y., Feng, G., 2011. Evolution of the total lightning activity in a leading-line and trailing stratiform mesoscale convective system over Beijing. Adv. Atmos. Sci. 28(4), 866. https://doi.org/10.1007/s00376–010–0001–8.

López, R.E., Otto, W.D., Ortiz, R., Holle, R.L., 1990. The lightning characteristics of convective cloud systems in northeastern Colorado. In Preprints, Conf. on Atmospheric Electricity, Kananaskis Park, AB, Canada, Amer. Meteor. Soc., pp. 727–731.

Luo, C., Chi, Y., Zhou, H., 2012. Characteristics of 3-D wind structure of Typhoon outer intensive banded echo using dual-doppler weather radar data. Atmos. Sci.

36(2), 247–258. doi:10.3878/j.issn.1006–9895.2011.10222. (In Chinese)

MacGorman, D.R., Burgess, D.W., 1994. Positive cloud-to-ground lightning in tornadic storms and hailstorms. Mon. Weather. Rev. 122(8), 1671–1697. https://doi.org/10.1175/1520–0493(1994)122<1671:PCTGLI>2.0.CO;2.

MacGorman, D.R., Burgess, D.W., Mazur, V., Rust, W.D., Taylor, W.L., Johnson, B. C., 1989. Lightning rates relative to tornadic storm evolution on 22 May 1981. J. Atmos. sci. 46(2), 221–251. https://doi.org/10.1175/1520–0469(1989)046<0221:LRRTTS>2.0.CO;2.

MacGorman, D.R., Rust, W.D., Schuur, T.J., Biggerstaff, M.I., Straka, J.M., Ziegler, C.L., Mansell, E.R., Bruning, E.C., Kuhlman, K.M., Lund, N.R., Biermann, N.S., Payne, C., Carey, L.D., Krehbiel, P.R., Rison, W., Eack, K.B., Beasley, W.H., 2008. TELEX the thunderstorm electrification and lightning experiment. Bull. Amer. Meteorol. Soc. 89(7), 997–1014. https://doi.org/10.1175/2007BAMS2352.1.

Martinez, M., 2002. The relationship between radar reflectivity and lightning activity at initial stages of convective storms. American Meteorological Society, 82nd Annual Meeting, First Annual Student Conference, Orlando, Florida, January 13.B.,

Mecikalski, R.M., Carey, L.D., 2018. Radar Reflectivity and Altitude Distributions of Lightning Flashes as a Function of Three Main Storm Types. J. Geophys. Res. 123(22), 12814, 128142https://doi.org/10.1029/2018JD029263.

Park, H.S., Ryzhkov, A.V., Zrnić, D.S., Kim, K.E., 2009. The hydrometeor classification algorithm for the polarimetric WSR-88D: Description and

Journal Pre-proof

application to an MCS. Weather Forecast. 24(3), 730 – 748. https://doi.org/10.1175/2008WAF2222205.1.

Pereyra, R.G., Avila, E.E., Castellano, N.E., Saunders, C.P., 2000. A laboratory study of graupel charging. J. Geophys. Res. Atmos. 105(D16), 20803 – 20812. https://doi.org/10.1029/2000JD900244.

Proctor, D.E., 1991. Regions where lightning flashes began. J. Geophys. Res. 96, 5099–5112. https://doi.org/10.1029/90JD02120.

Rudlosky, S.D., Fuelberg, H.E., 2010. Pre-and postupgrade distributions of NLDN reported cloud-to-ground lightning characteristics in the contiguous United States. Mon. Weather. Rev. 138(9), 3623 – 3633. https://doi.org/10.1175/2010MWR3283.1.

Rust, W.D., MacGorman, D.R., Bruning, E.C., Weiss, S.A., Krehbiel, P.R., Thomas, R.J., Rison, W., Hamlin, T., Harlin, J., 2005. Inverted-polarity electrical structures in thunderstorms in the Severe Thunderstorm Electrification and Precipitation Study (STEPS). Atmos. Res., 76(1), 247ical https://doi.org/10.1016/j.atmosres.2004.11.029.

Shao, X.M., Krehbiel, P.R., 1996. The spatial and temporal development of intracloud lightning. J. Geophys. Res. Atmos. 101(D21), 26641 – 26668. https://doi.org/10.1029/96JD01803.

Shi, D., Zheng, D., Zhang, Y., Zhang, Y., Huang, Z., Lu, W., Chen, S., Yan, X., 2017. Low-frequency E-field Detection Array (LFEDA)—Construction and preliminary results. Sci. China-Earth Sci. 60(10), 1896 – 1908.

https://doi.org/10.1007/s11430–016–9093–9.

Soula, S., Seity, Y., Feral, L., Sauvageot, H., 2004. Cloud-to-ground lightning activity in hail - bearing storms. J. Geophys. Res. Atmos. 109(D2). https://doi.org/10.1029/2003JD003669.

Suzuki, T. 1992. Long term observation of winter lightning on Japan Sea coast. Res. Lett. Atmos. Electr. 12, 53–56.

Takahashi, T., 1978. Riming electrification as a charge generation mechanism in thunderstorms. J. Atmos. Sci. 35(8), 1536–1548. https://doi.org/10.1175/1520–0469(1978)035<1536:REAACG>2.0.CO;2.

Takeuti, T., Nakano, M., Yamamoto, Y., 1976. Remarkable characteristics of cloud-to-ground discharges observed in winter thunderstorms in Hokuriku area, Japan. J. Meteorol. Soc. Jpn. Ser. II, 54(6), 436 – 440. https://doi.org/10.2151/jmsj1965.54.6_436.

Tian, F., Zheng, Y., Zhang, X., Zhang, T., Lin, Y., Zhang, X., Zhu, W., 2018. Structure, triggering and maintenance mechanism of convective systems during the Guangzhou extreme rainfall on 7 May 2017. Meteor Mon, 44(4), 469–484. https://doi.org/10.7519/j.issn.1000–0526.2018.04.001.(in Chinese)

Ventura, J.F., Pineda, N., Besic, N., Grazioli, J., Hering, A., Der Velde, O.A., Romero, D., Sunjerga, A., Mostajabi, A., Azadifar,M., Rubinstein,M., Montanya, J., Germann, U., Rachidi, F., 2019. Polarimetric radar characteristics of lightning initiation and propagating channels. Atmos. Meas. Tech., 12(5), 2881–2911, https://doi.org/105194/amti.org/ch., 12(

Vincent, B.R., Carey, L.D., Schneider,D., Keeter, K., Gonski, R., 2003. Using WSR-88D reflectivity data for the prediction of cloud-to-ground lightning: A central North Carolina study. Nat. Wea. Digest. 27, 35–44.

Wang, F., Zhang, Y., Zhao, J., Lv, W., Meng, Q., 2008. The preliminary application of radar data to the lightning warning of isolated storm cells. J. Appl. Meteorol. Sci. 19(2), 153(2), 1(In Chinese). https://doi.org/10.3969/j.issn.1001-7313.2008.02.004

Wang, F., Zhang, Y., Zheng, D., Xu, L., 2015. Impact of the vertical velocity field on charging processes and charge separation in a simulated thunderstorm. J. Meteorol. Res. 29(2), 328–343. https://doi.org/10.1007/s13351–015–4023–0.

Williams, E. R., 1989. The tripole structure of thunderstorms. J. Geophys. Res. Atmos. 94(D11), 13151–13167. https://doi.org/10.1029/JD094iD11p13151.

Wu, C., Liu, L., Wei, M., Xi, B., Yu, M., 2018. Statistics-based optimization of the polarimetric radar hydrometeor classification algorithm and its application for a squall line in South China. Adv. Atmos. Sci. 35(3), 296 – 316. https://doi.org/10.1007/s00376–017–6241–0.

Wu, T., Yoshida, S., Akiyama, Y., Stock, M., Ushio, T., Kawasaki, Z., 2015. Preliminary breakdown of intracloud lightning: Initiation altitude, propagation speed, pulse train characteristics, and step length estimation. J. Geophys. Res. Atmos. 120(18), 9071–9086. https://doi.org/10.1002/2015JD023546.

Xu, J., Bi, B., Shen, Y., Chen, T., Gong, Y., Li, J., 2018. Mesoscale characteristics and mechanism analysis of the unexpected local torrential rain in Guangzhou on 7

May 2017. Acta. Meteorol. Sin. 76(4), 511 – 524. (In Chinese). http://dx.doi.org/10.11676/qxxb2018.016.

Xu, S., Zheng, D., Wang, Y., Hu, P., 2016. Characteristics of the two active stages of lightning activity in two hailstorms. J. Meteorol. Res. 30(2), 265 – 281. https://doi.org/10.1007/s13351–016–5074–6.

Zeng, Z., Shen, Y., Zhu, K., Li, S., 2018.Mesoscale characteristic analysis and primary discussion on the formation of the 7 May 2017 torrential rainfall in Guangzhou. J. Tro. Meteorol. 34(6), 791 – 805. (In Chinese). doi:10.16032/j.issn.1004–4965.2018.06.008.

Zhang, A., Xiao, L., Min, C., Chen, S., Kulie, M., Huang, C., Liang, Z., 2019. Evaluation of latest GPM-Era high-resolution satellite precipitation products during the May 2017 Guangdong extreme rainfall event. Atmos. Res. 216, 76–85. https://doi.org/10.1016/j.atmosres.2018.09.018.

Zhang, Y., Liu, L., Wen, H., Wu, C., Zhang, Y., 2018. Evaluation of the polarimetric-radar quantitative precipitation estimates of an extremely heavy rainfall event and nine common rainfall events in Guangzhou. Atmos. 9(9). https://doi.org/10.3390/atmos9090330.

Zhang, Y., Meng, Q., Krehbiel, P.R., Liu, X., Yan, M., Zhou, X., 2006a. Spatiotemporal characteristics of positive cloud-to-ground lightning discharges and bidirectional leader of the lightning. Sci. China. Ser. D. 49(2), 212–224. https://doi.org/10.1007/s11430–005–0054–1.

Zhang, Y., Meng, Q., Lu, W., Krehbiel, P.R., Liu, X., Zhou, X., 2006b. Charge structures and cloud-to-ground lightning discharges characteristics in two supercell thunderstorms. Chin. Sci. Bull. 51(2), 198 – 212. https://doi.org/10.1007/s11434–005–0233–7.

Zhang, Z., Zheng, D., Zhang, Y., Lu, G., 2017. Spatial–temporal characteristics of lightning flash size in a supercell storm. Atmos. Res. 197, 201 – 210. https://doi.org/10.1016/j.atmosres.2017.06.029.

Zheng, D., MacGorman, D.R., 2016. Characteristics of flash initiations in a supercell cluster with tornadoes. Atmos. Res. 167, 249 – 264. https://doi.org/10.1016/j.atmosres.2015.08.015.

Zheng, D., Shi, D., Zhang, Y., Zhang, Y., Lyu, W., Meng, Q., 2019b. Initial leader properties during the preliminary breakdown processes of lightning flashes and their associations with initiation positions. J. Geophys. Res. Atmos. https://doi.org/10.1029/2019JD030300.

Zheng, D., Wang, D., Zhang, Y., Wu, T., Takagi, N., 2019a. Charge regions indicated by LMA lightning flashes in Hokuriku's winter thunderstorms. J. Geophys. Res. Atmos. 124(13), 7179-7206. https://doi.org/10.1029/2018JD030060.

Zheng, D., Zhang, Y., Meng, Q., 2018. Properties of negative initial leaders and lightning flash size in a cluster of supercells. J. Geophys. Res. Atmos. 123(22), 12,857–12,876. https://doi.org/10.1029/2018JD028824.

Zheng, D., Zhang, Y., Meng, Q., Chen, L., Dan, J., 2016. Climatological comparison of small-and large-current cloud-to-ground lightning flashes over southern China. J. Clim. 29(8), 2831–2848. https://doi.org/10.1175/JCLI–D–15–0386.1.

Zheng, D., Zhang, Y., Meng, Q., Lu, W., Yi, X., 2009. Total lightning characteristics and electric structure evolution in a hailstorm. J. Meteorol. Res. 23(2), 233–249.

Zheng, D., Zhang, Y., Meng, Q., Lu, W., Zhong, M., 2010. Lightning activity and electrical structure in a thunderstorm that continued for more than 24 h. Atmos. Res. 97(1–2), 241–256. https://doi.org/10.1016/j.atmosres.2010.04.011.

Liu Ze: Validation, Formal analysis, Investigation, Writing - Original Draft, Visualization

Dong Zheng: Conceptualization, Methodology, Software, Data Curation, Writing - Review & Editing, Project administration, Funding acquisition

Fengxia Guo: Supervision, Writing - Review & Editing, Funding acquisition

Yang Zhang: Resources, Data Curation, Software

Yijun Zhang: Supervision, Writing - Review & Editing

Chong Wu: Resources, Data Curation

Haonan Chen: Resources, Data Curation

Songyu Han: Resources, Data Curation

Declaration of interests

☒ The authors declare that they have no known competing financial interests or personal relationships that could have appeared to influence the work reported in this paper.

☐The authors declare the following financial interests/personal relationships which may be considered as potential competing interests:

Highlights:

- Investigating electrical characteristics in a rainstorm dominated by warm cloud precipitation is novel.
- In this rainstorm, lightning discharges predominately occurred in areas featuring dry snow and relatively weak precipitation.
- The lightning discharges spatially deviate from the origin area of charging; the cause of this is discussed.

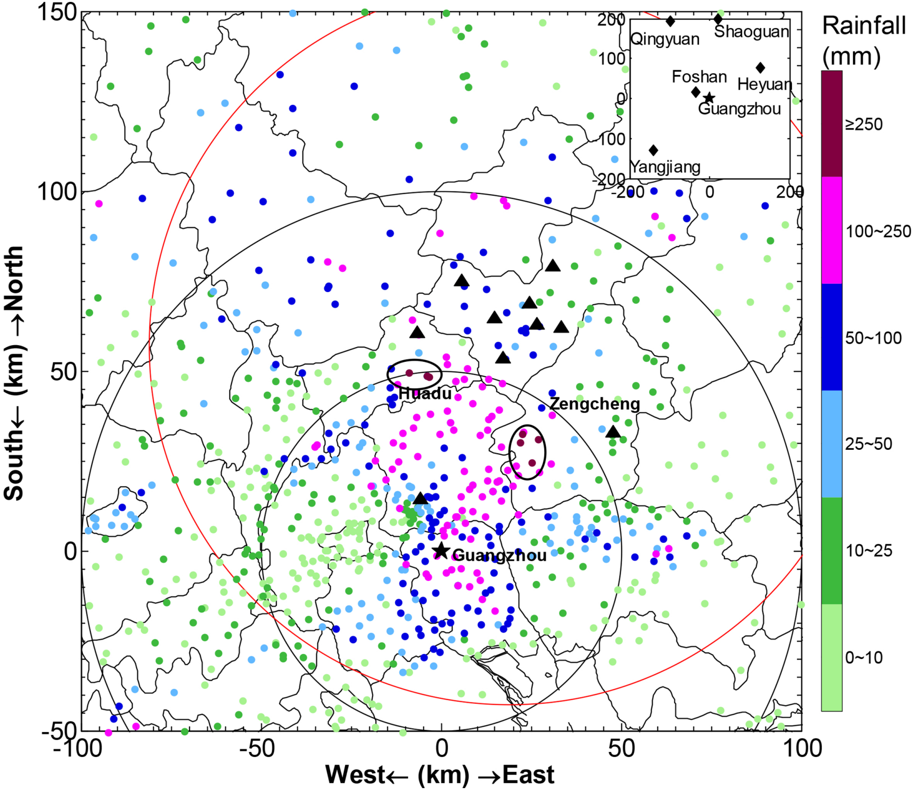
Rainfall (mm)
≥250
100~250
50~100
25~50
10~25
0~10
Qingyuan
Shaoguan
Foshan
Heyuan
Guangzhou
Yangjiang
Huadu
Zengcheng
Guangzhou
South← (km) →North
West← (km) →East

Figure 1

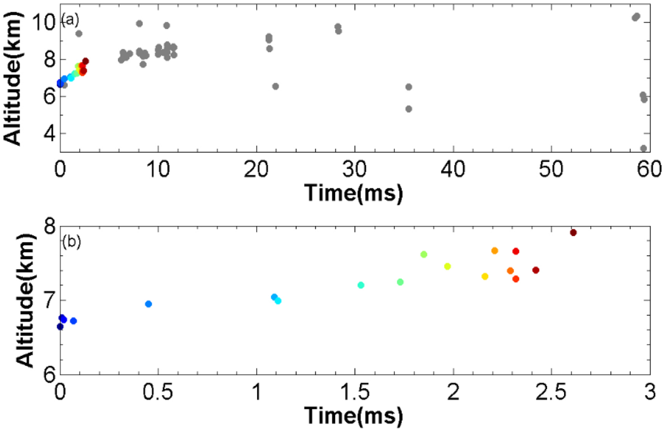

(a)
Altitude(km)
10
8
6
4
0
10
20
30
40
50
60
Time(ms)
(b)
Altitude(km)
8
7
6
0
0.5
1
1.5
2
2.5
3
Time(ms)

Figure 2

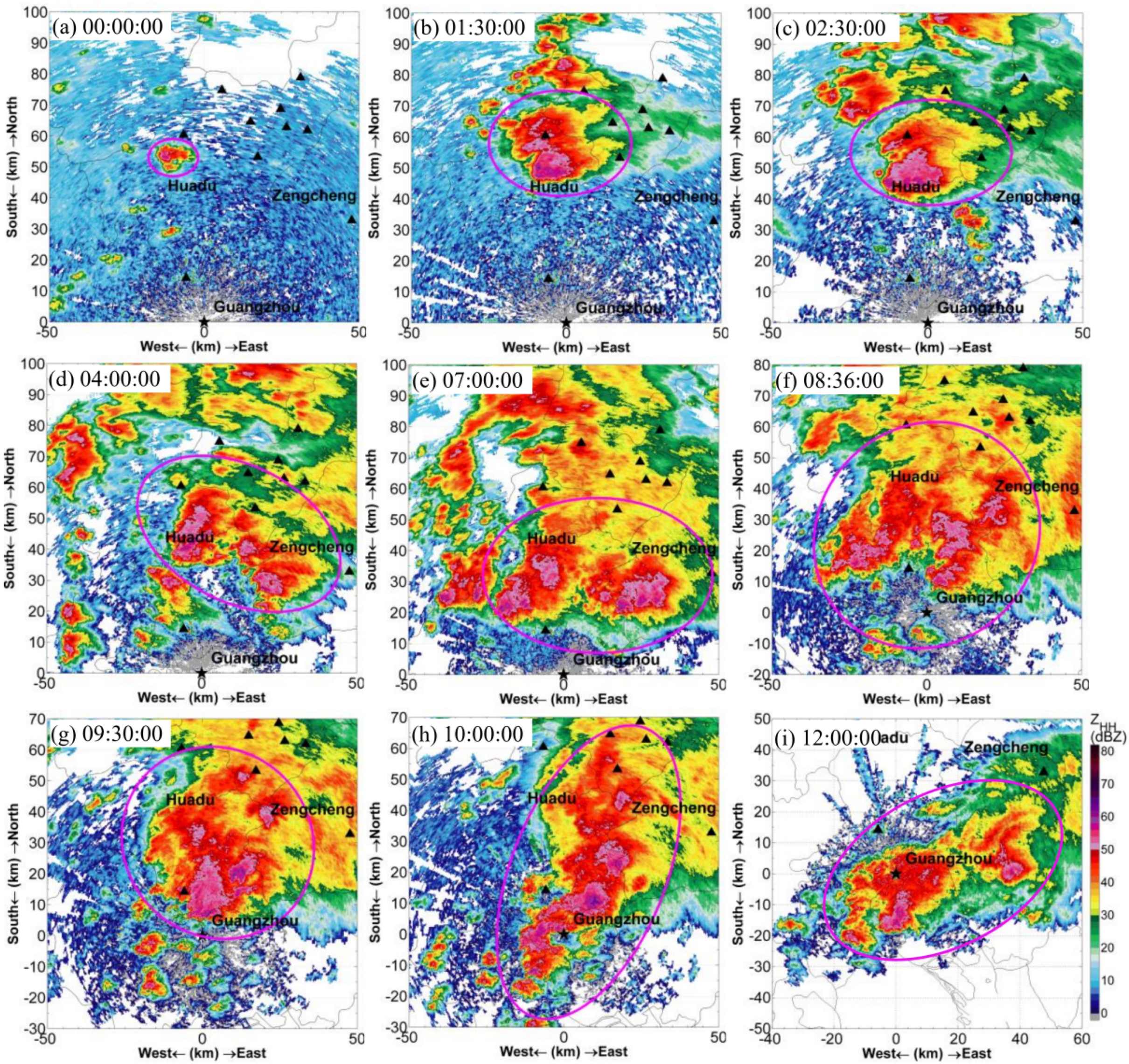

(a) 00:00:00
(b) 01:30:00
(c) 02:30:00
(d) 04:00:00
(e) 07:00:00
(f) 08:36:00
(g) 09:30:00
(h) 10:00:00
(i) 12:00:00
Huadu
Zengcheng
Guangzhou
South← (km) →North
West← (km) →East
Z_HH (dBZ)

Figure 3

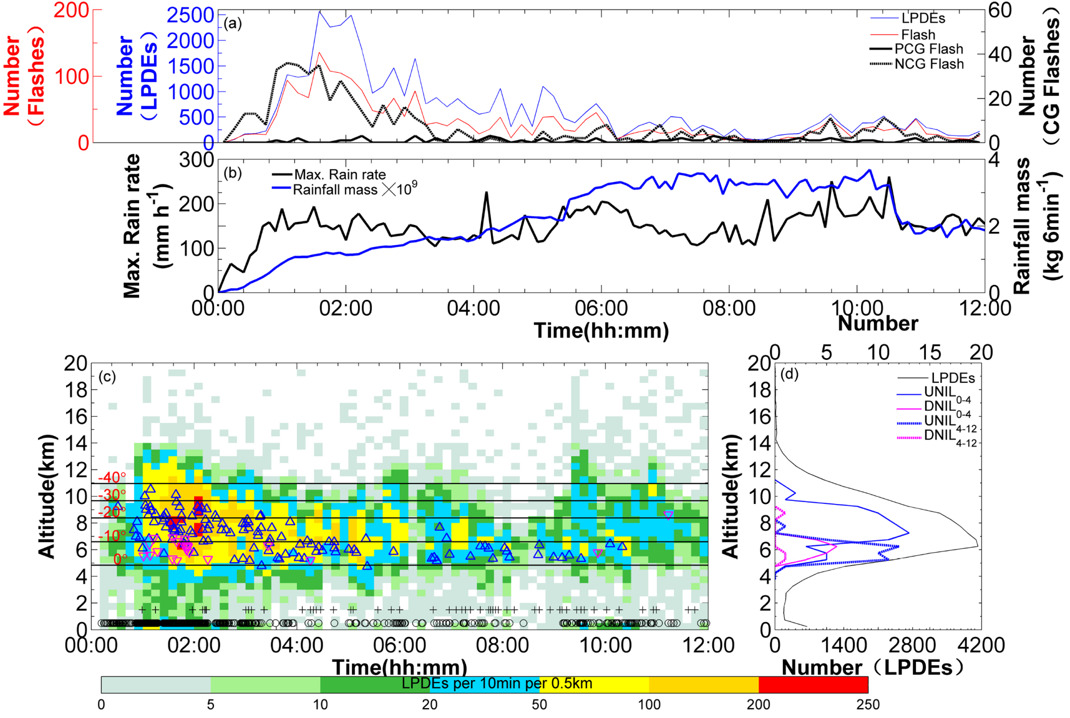

(a)
Number (Flashes)
Number (LPDEs)
Number (CG Flashes)
LPDEs
Flash
PCG Flash
NCG Flash
(b)
Max. Rain rate
Rainfall mass ×10^9
Max. Rain rate (mm h^-1)
Rainfall mass (kg 6min^-1)
Time(hh:mm)
(c)
-40°
-30°
-20°
-10°
0°
Altitude(km)
Time(hh:mm)
LPDEs per 10min per 0.5km
(d)
Number
LPDEs
UNIL 0-4
DNIL 0-4
UNIL 4-12
DNIL 4-12
Altitude(km)
Number (LPDEs)

Figure 4

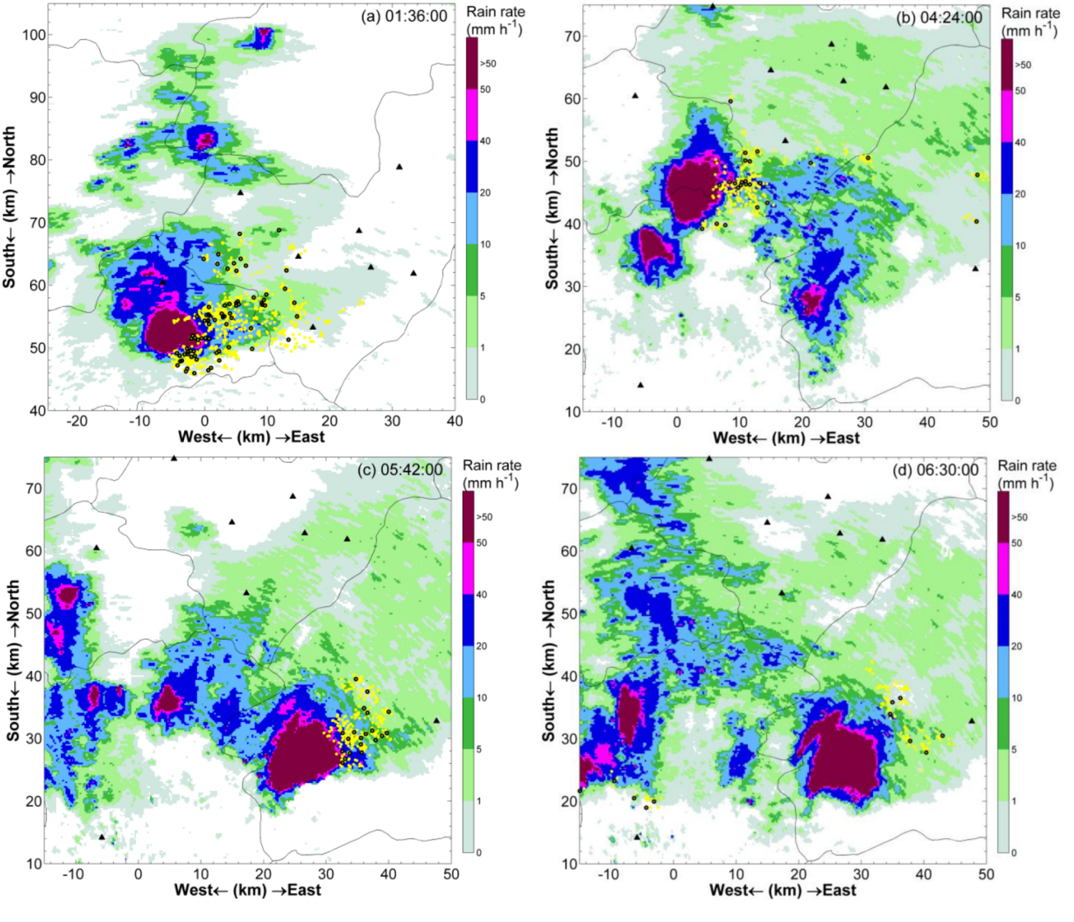
(a) 01:36:00
(b) 04:24:00
(c) 05:42:00
(d) 06:30:00
Rain rate (mm h-1)
>50
50
40
20
10
5
1
0
South← (km) →North
West← (km) →East

Figure 5

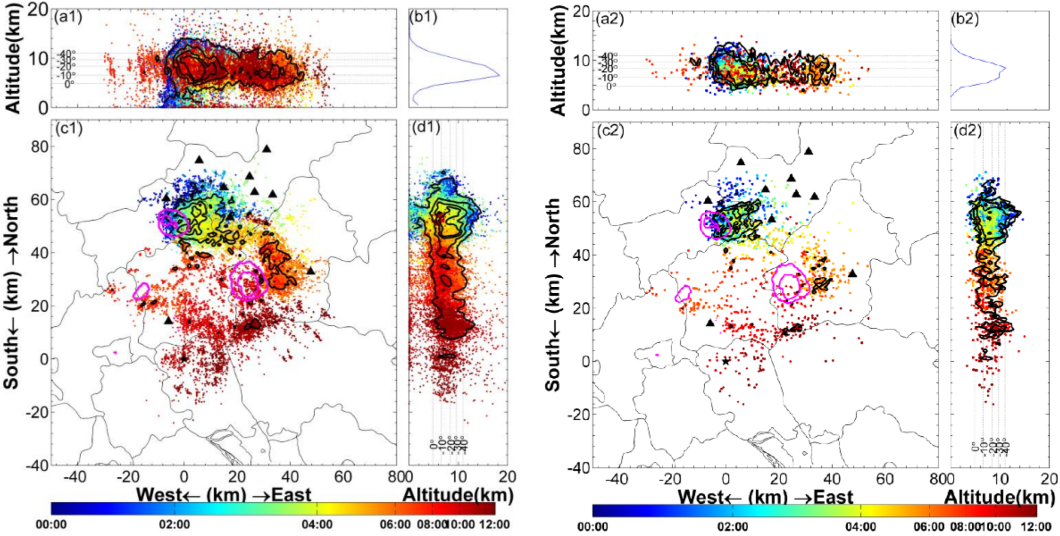
(a1)
(b1)
(c1)
(d1)
(a2)
(b2)
(c2)
(d2)
Altitude(km)
South← (km) →North
West← (km) →East
Altitude(km)
00:00
02:00
04:00
06:00
08:00
10:00
12:00

Figure 6

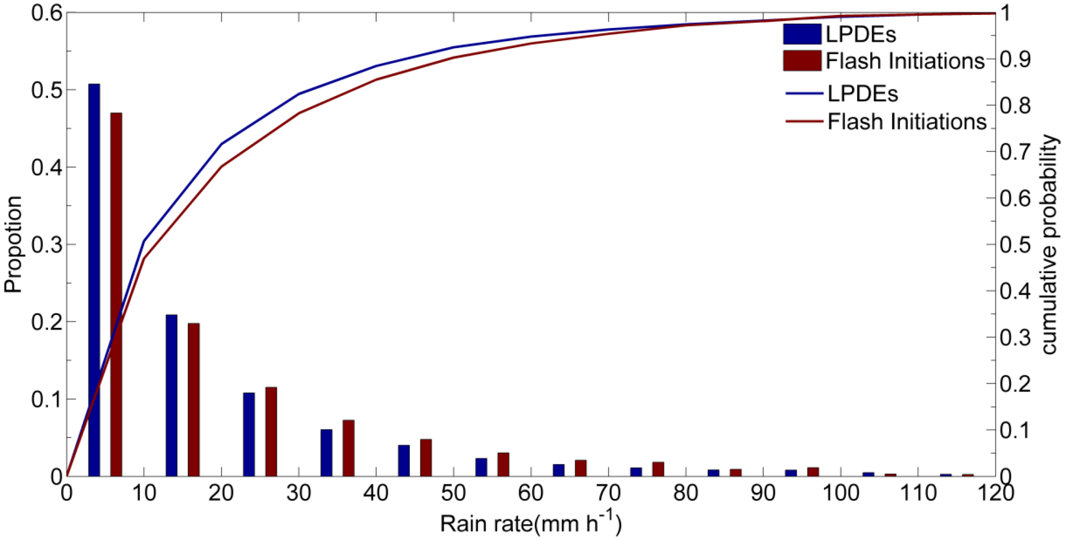

0.6
0.5
0.4
0.3
0.2
0.1
0
Propotion
1
0.9
0.8
0.7
0.6
0.5
0.4
0.3
0.2
0.1
0
cumulative probability
0
10
20
30
40
50
60
70
80
90
100
110
120
Rain rate(mm h^{-1})
LPDEs
Flash Initiations
LPDEs
Flash Initiations

Figure 7

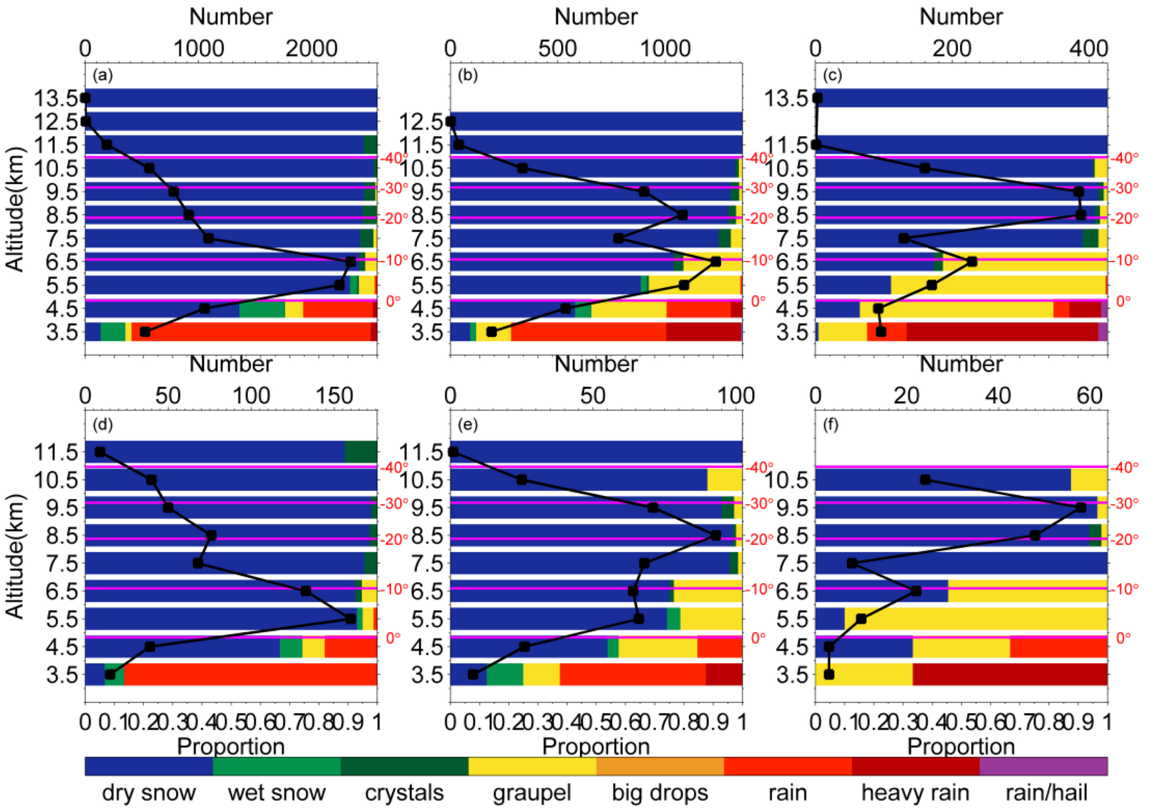

Number
Altitude(km)
Proportion
(a)
(b)
(c)
(d)
(e)
(f)
-40°
-30°
-20°
-10°
0°
dry snow
wet snow
crystals
graupel
big drops
rain
heavy rain
rain/hail

Figure 8

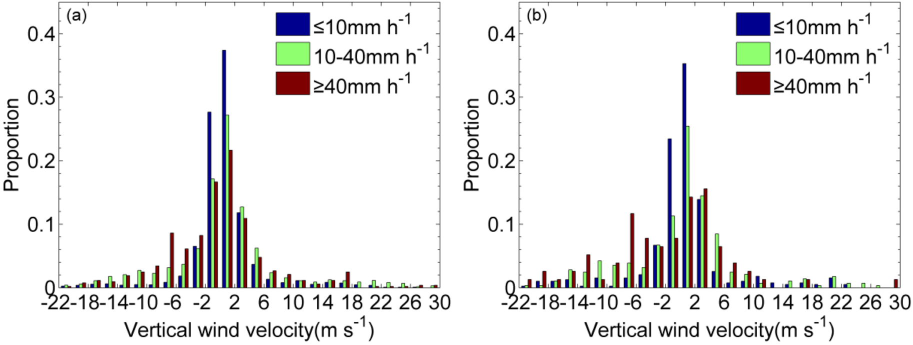

(a)
≤10mm h-1
10-40mm h-1
≥40mm h-1
Proportion
0.4
0.3
0.2
0.1
0
-22 -18 -14 -10 -6 -2 2 6 10 14 18 22 26 30
Vertical wind velocity(m s-1)
(b)
≤10mm h-1
10-40mm h-1
≥40mm h-1
Proportion
0.4
0.3
0.2
0.1
0
-22 -18 -14 -10 -6 -2 2 6 10 14 18 22 26 30
Vertical wind velocity(m s-1)

Figure 9

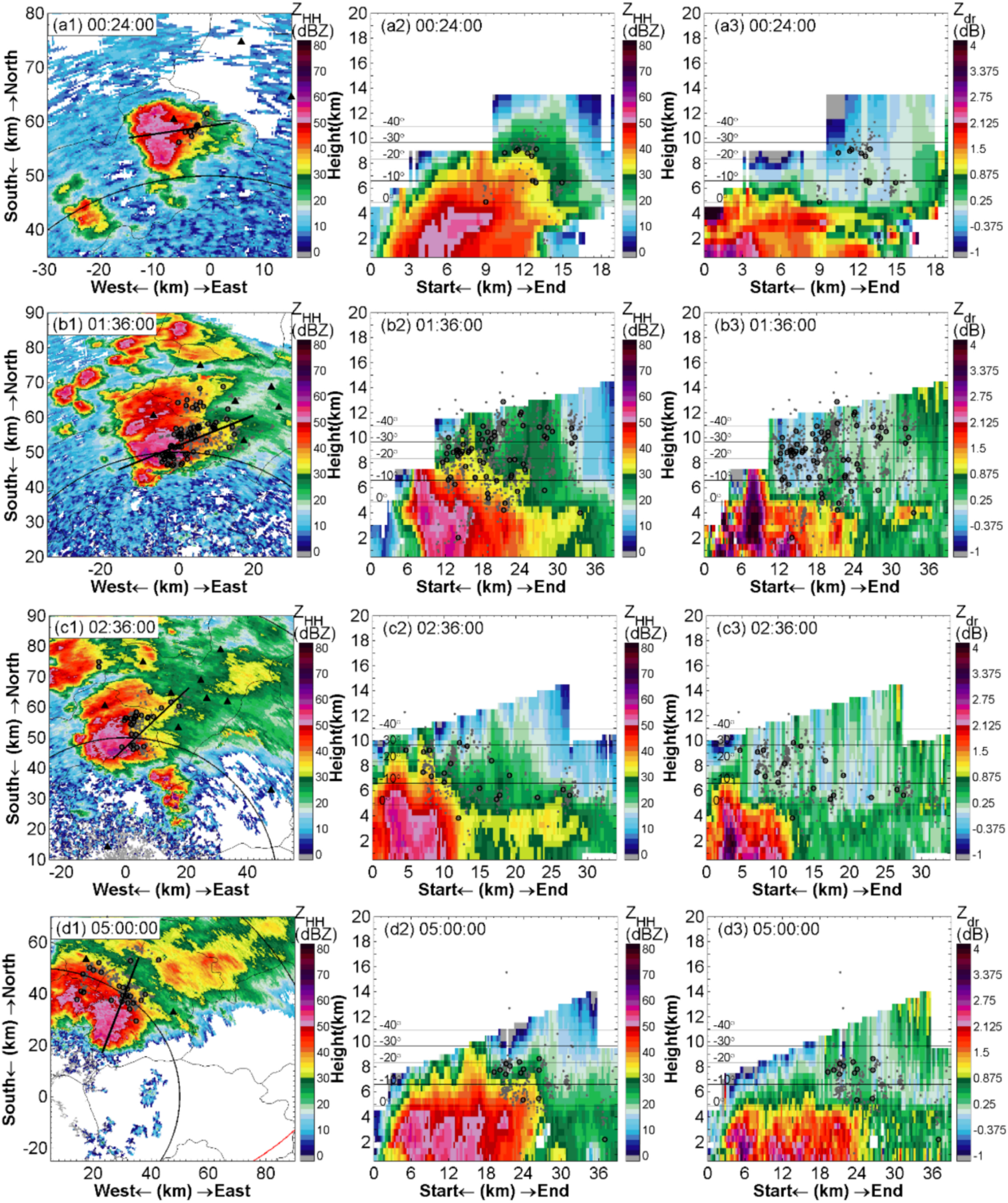
(a1) 00:24:00
(a2) 00:24:00
(a3) 00:24:00
(b1) 01:36:00
(b2) 01:36:00
(b3) 01:36:00
(c1) 02:36:00
(c2) 02:36:00
(c3) 02:36:00
(d1) 05:00:00
(d2) 05:00:00
(d3) 05:00:00
South← (km) →North
West← (km) →East
Height(km)
Start← (km) →End
ZHH (dBZ)
Zdr (dB)

Figure 10

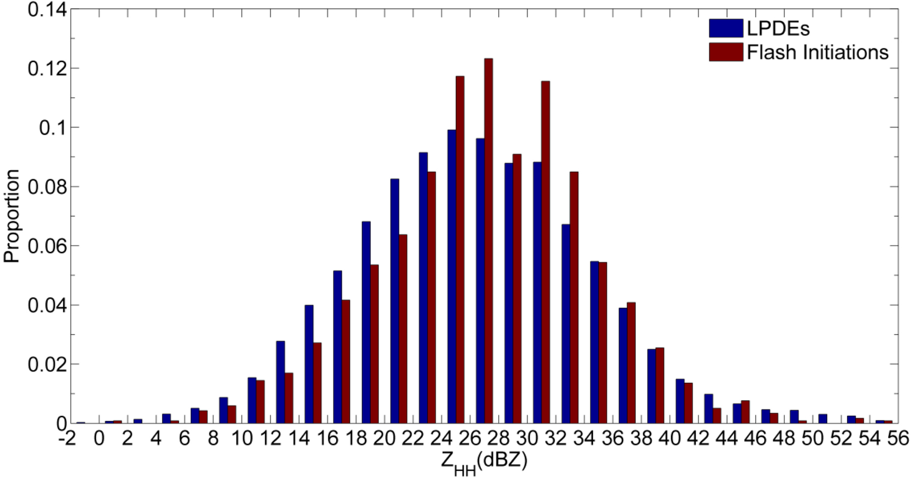

LPDEs
Flash Initiations
Proportion
0.14
0.12
0.1
0.08
0.06
0.04
0.02
0
-2 0 2 4 6 8 10 12 14 16 18 20 22 24 26 28 30 32 34 36 38 40 42 44 46 48 50 52 54 56
Z_{HH}(dBZ)

Figure 11

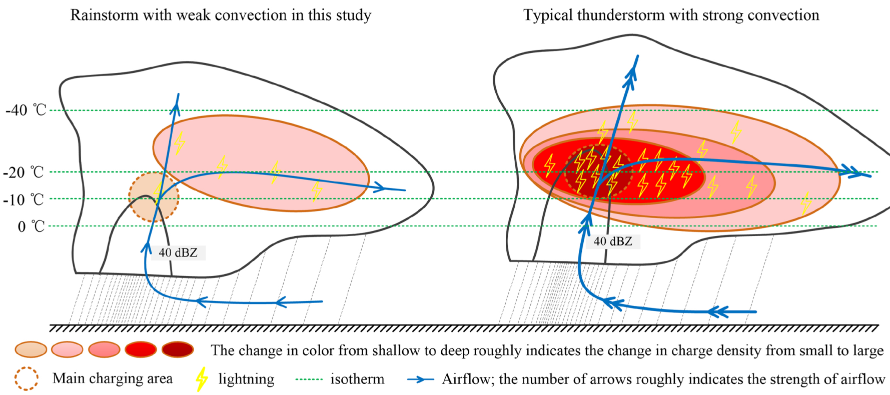
Rainstorm with weak convection in this study
Typical thunderstorm with strong convection
-40 ℃
-20 ℃
-10 ℃
0 ℃
40 dBZ
40 dBZ
The change in color from shallow to deep roughly indicates the change in charge density from small to large
Main charging area
lightning
isotherm
Airflow; the number of arrows roughly indicates the strength of airflow

Figure 12